Front. Optoelectron. 2019, 12(2): 117–147
https://doi.org/10.1007/s12200-018-0860-7

REVIEW ARTICLE

Terahertz wave generation from ring-Airy beam induced plasmas and remote detection by terahertz-radiation-enhanced-emission-of-fluorescence: a review

Kang LIU[1], Pingjie HUANG[2], Xi-Cheng ZHANG (✉)[1,3]

1 The Institute of Optics, University of Rochester, Rochester, NY 14627, USA
2 State Key Laboratory of Industrial Control Technology, College of Control Science and Engineering, Zhejiang University, Hangzhou 310027, China
3 The Beijing Advanced Innovation Center for Imaging Technology, Capital Normal University, Beijing 100037, China

Abstract With the increasing demands for remote spectroscopy in many fields ranging from homeland security to environmental monitoring, terahertz (THz) spectroscopy has drawn a significant amount of attention because of its capability to acquire chemical spectral signatures non-invasively. However, advanced THz remote sensing techniques are obstructed by quite a few factors, such as THz waves being strongly absorbed by water vapor in the ambient air, difficulty to generate intense broadband coherent THz source remotely, and hard to transmit THz waveform information remotely without losing the signal to noise ratio, etc. In this review, after introducing different THz air-photonics techniques to overcome the difficulties of THz remote sensing, we focus mainly on theoretical and experimental methods to improve THz generation and detection performance for the purpose of remote sensing through tailoring the generation and detection media, air-plasma.

For the THz generation part, auto-focusing ring-Airy beam was introduced to enhance the THz wave generation yield from two-color laser induced air plasma. By artificially modulated exotic wave packets, it is exhibited that abruptly auto-focusing beam induced air-plasma can give an up to 5.3-time-enhanced THz wave pulse energy compared to normal Gaussian beam induced plasma under the same conditions. At the same time, a red shift on the THz emission spectrum is also observed. A simulation using an interference model to qualitatively describe these behaviors has be developed.

For the THz detection part, the results of THz remote sensing at 30 m using THz-radiation-enhanced-emission-of-fluorescence (THz-REEF) technique are demonstrated, which greatly improved from the 10 m demonstration last reported. The THz-REEF technique in the counter-propagation geometry was explored, which is proved to be more practical for stand-off detections than co-propagation geometry. We found that in the counter-propagating geometry the maximum amplitude of the REEF signal is comparable to that in the co-propagating case, whereas the time resolved REEF trace significantly changes. By performing the study with different plasmas, we observed that in the counter-propagating geometry the shape of the REEF trace depends strongly on the plasma length and electron density. A new theoretical model suggesting that the densest volume of the plasma does not contribute to the fluorescence enhancement is proposed to reproduce the experimental measurements.

Our results further the understanding of the THz-plasma interaction and highlight the potential of THz-REEF technique in the plasma detection applications.

Keywords ultrafast terahertz (THz) techniques, THz air-photonics, ring-Airy beams, THz-radiation-enhanced-emission-of-fluorescence (THz-REEF) of air-plasma in co-propagation geometry, THz-REEF of air-plasma in counter-propagation geometry

1 Introduction

1.1 Background

Terahertz (THz) wave is the electromagnetic wave with the frequencies lying between microwave and infrared regions of the spectrum band (1 THz = 10^{12} Hz). It has also been called "T-ray," where "T" stands for terahertz indicating its strong potential in the imaging applications [1,2]. Common definition of THz frequencies includes the

Received September 2, 2018; accepted October 13, 2018

E-mail: xi-cheng.zhang@rochester.edu

Invited Paper

spectral range between 0.1 – 10 THz. The frequency below or beyond this range can also be loosely defined as THz waves in some cases.

Many objects around us, including our human bodies, thermally radiate electromagnetic waves that partially fall into THz frequencies. As a matter of fact, cosmic background radiation, the residue from the Big Bang, has a maximum spectral radiance at 160 GHz [1–5]. However, most of the naturally incurred THz radiation sources are incoherent, which can hardly be used scientifically. Due to the lack of bright coherent THz sources and effective detection technologies, for a long time in history, THz frequencies were underdeveloped and stayed relatively unfamiliar to people. A "THz gap" in the electromagnetic spectrum band remained barely touched until 1980s, when ultrafast optoelectronics and microscopic semiconductors started to thrive, bringing the crucial technologies for studying the THz frequencies.

The "THz gap" was not completely a historical accident, but a consequence of its special position in the electromagnetic spectrum. The study of THz waves, unfortunately, does not easily fit into either of the fields of Electronics or Photonics [2]. For example, in Electromagnetics, the wavelengths of microwaves and radio waves are normally much larger than the physical size of the electronics elements, so the electric and magnetic field can be considered approximately uniform on the elements. In Optics, it is usually the opposite case: the optical wavelengths are much smaller than certain dimension of the optical elements, so the transporting medium can be considered uniform to the photons. To study THz waves, the knowledge of the two fields must be combined to develop new tools and principles.

Bridging the "THz gap" is not the only reason drawing the attention from researchers. THz wave's many special properties that gift it with broad range of potential applications are the real attractions. Former research has revealed that there are many important features in THz waves, such as transparency to dielectric materials [1,2,6–11], non-destructiveness [12–14], spectroscopic fingerprinting [15], and so on.

Other than many interesting applications, THz technology also has its limitation and challenges. For example, THz wave is difficult to pass through conductive materials, thus makes it not easy to inspect objects shielded by metal. Liquid with strong polarity, such as water, has substantial absorption of THz radiation, which is another challenge of THz technology and blocks up its application in biomedicine. THz remote sensing may have advantages in Mie scattering, but the strong absorption of THz radiation by water vapor in the air has hindered the development of this technology. This review would try to discuss the theoretical and experimental study of remotely generating and detecting of THz wave by tailoring Airy plasmas.

1.2 Ultrafast terahertz techniques

1.2.1 Terahertz generation

The development of efficient, robust, broadband, and coherent THz sources is constantly pushing the frontier of THz science and technology forward, enabling new research and applications, especially for the fields to reveal nonlinear phenomena that require ultra-intense THz radiations [16]. Before discussing the concerned THz remote generation technologies, broadband THz pulse generation technologies that involve several different ultrafast optical methods will be introduced briefly.

1) Photoconductive antenna

Broadband THz pulses can be generated by a biased photoconductive (PC) antenna excited with femtosecond optical pulses. The PC antenna is one of the most widely used components for THz generation and detection. A typical THz generation PC antenna structure. It is composed of two metal electrodes deposited on a semiconductor substrate [17,18]. When generating THz radiation, a DC voltage is applied across the electrodes. The femtosecond optical pulses which have photon energy higher than the semiconductor energy band gap will radiate the area between the electrodes and generate photo-induced free carriers in the substrate. Sometimes, free carriers can also be formed using excitation pulses with photon energy lower than the semiconductor band gap, due to multi-photon absorption in the substrate. Once the free carriers are formed, they will be accelerated by the electric field between the electrodes, and a photocurrent J is produced. As the photocurrent varies with time, it radiates electromagnetic wave pulses with an electric field E_{THz} at the far field that can be expressed as [1]

$$E_{\mathrm{THz}} \propto \frac{\partial J(t)}{\partial t}. \tag{1}$$

The emitted THz electric field has a polarization parallel to the direction of the bias field, which can be flipped by switching the direction of the bias field. The power and bandwidth of the THz emission from PC antenna largely depend on the structure of the electrodes [19]. The output power of a PC emitter also depends on the bias voltage and the optical pump power. When the optical pump power is low and the bias field is weak, the THz radiation field amplitude increases linearly with these two parameters. However, increasing the bias voltage has a limitation because a high electric field may result in the breakdown of the substrate material.

In addition, the THz radiation output power will saturate as the optical pump power reaches a certain level, for the screening effect of the bias field by the photo-induced carriers.

Ever since the first introduction of THz generation by PC antenna in the 1980s [20], this technique has undergone dramatic developments, due to the soaring amount of research on the THz-time-domain-spectroscopy techniques. Up to now, the strongest broadband THz pulse energy emitted by PC antenna was reported to be 8.3 μJ with a peak electric field of 331 kV/cm, achieved with an encapsulated interdigitated ZnSe Large Aperture Photo-Conductive Antenna (LAPCA) [21].

2) Optical rectification

Optical rectification (OR) is a second order nonlinear effect that is widely exploited for broadband THz pulse generation. Compared with PC antennae, OR crystals do not require application of high voltage on the material, making it one of the most efficient and convenient intense coherent broadband table-top THz sources [22].

In essence, OR is the generation of a quasi-DC polarization in a nonlinear material when it has been passed through by an intense optical beam, which results in a DC electric field proportional to the beam intensity. It can be understood as a second order phenomenon that is the reverse process of the electro-optic effect. If the light beam that induces OR is a pulse instead of a continuous wave, the electric field generated by OR will become a time varying function related with the pulse envelope, thus radiate electromagnetic waves. The far field radiation electric field should be proportional to the second derivative of OR induced time varying electric field.

$$E_{\mathrm{THz}}(t) \propto \frac{\partial^2 P(0,t)}{\partial t^2} = \chi^{(2)} \frac{\partial^2 I(t)}{\partial t^2}. \tag{2}$$

Here, $I(t)$ is the time dependent optical beam intensity, $P(0)$ is the second orderelectric polarization induced by OR, and $\chi^{(2)}$ is known as the second-order nonlinear optical susceptibility. When the optical pulse duration is in picosecond or sub-picosecond level, the radiation frequency is within THz range.

Due to the fact that the second order nonlinear susceptibility $\chi^{(2)}$ vanishesin the centrosymmetric medium [23], OR requires the material to have a noncentrosymmetric structure, such as the zinc-blended structure. The typical zinc-blended crystals that have been used in THz generations and detections include ZnTe, GaAs, GaP, etc.

Other than the susceptibility that is based on the crystal structure, the THz radiation efficiency, waveform and bandwidth depend on many factors, including laser beam properties, phase matching conditions, crystal thickness, orientation, absorption and dispersion, etc. In a nonlinear process such as optical rectification, one of the most crucial factors is the phase matching condition, which requires the energy and momentum conservation of the participating electromagnetic waves [24,25].

For OR THz generation process, it can be described as follows:

$$\begin{cases} \omega_{\mathrm{O1}} - \omega_{\mathrm{O2}} = \Omega_{\mathrm{THz}}, \\ k_{\mathrm{O1}} - k_{\mathrm{O2}} = k_{\mathrm{THz}}, \end{cases} \tag{3}$$

where ω_{O1} and ω_{O2} are the two frequency components that participate in the OR, k_{O1} and k_{O2} are their corresponding wave vectors. If we divide the first equation with the second one, we get

$$\frac{\partial \omega_{\mathrm{O}}}{\partial k_{\mathrm{O}}} = \frac{\Omega_{\mathrm{THz}}}{\Omega k_{\mathrm{THz}}}, \tag{4}$$

$$v_{\mathrm{G,O}} = v_{\mathrm{Ph,THz}}, \tag{5}$$

where $v_{\mathrm{G,O}}$ is the group velocity of the optical pulse, and $v_{\mathrm{Ph,THz}}$ is the phasevelocity of THz.

When the optical pulse group velocity equals the phase velocity of THz wave, the phase matching condition of OR THz generation is satisfied. For THz generation ZnTe is one of the most popular crystals [26], because in this material the group velocity of femtosecond laser pulse around 800 nm (Ti:sapphire laser center wavelength) matches very well with phase velocity of THz wave.

3) Tilted pulse front

ZnTe crystal's electro-optic (EO) coefficient is relatively small compared with some other crystals, such as inorganic EO crystal $LiNbO_3$ and organic crystal 4-N-methlystibazolium tosylate (DAST) [22]. THz generation from $LiNbO_3$ based on the tilted pulse front techniques would be introduced in this section.

In 1971 Yang et al. first demonstrated the THz generation by OR with picosecond laser pulses, using $LiNbO_3$ crystal as the excited material [27]. However, the conventional OR method of sending the pump beam at normal incidence to the crystal and generating THz radiation in the forward direction does not work efficiently with $LiNbO_3$, due to the large mismatch between the optical group velocity and the THz phase velocity in the material. The optical group refractive index is n_{O} = 2:3, and the THz refractive index is n_{T} = 5:2 [17]. To conquer this mismatch, in 2002 Hebling et al. proposed the pulse front tilting technique [28], which later became a standard procedure for THz generation from $LiNbO_3$ crystal.

In analogy to the Cherenkov radiation, in $LiNbO_3$, a femtosecond laser beam with considerably smaller beam size than the THz wavelength can be seen as a point source moving faster than the THz radiation. If the optical beam size is not negligible compared to THz wavelength, when the pulse front is aligned with the Cherenkov cone, the optical pulse front will propagate with the THz radiation at the same speed. Therefore, the velocity matching is fulfilled. The Cherenkov cone angle θ_{c} can be calculated using the optical group and THz phase refractive indices in

$LiNbO_3$ as follows:

$$\theta_c = \cos^{-1}\left(\frac{v_T}{v_O}\right) = \cos^{-1}\left(\frac{n_T}{n_O}\right) \simeq 64^\circ. \quad (6)$$

The tilt of the optical pulse front can be achieved with a diffractive grating [29]. After the grating, an imaging system can be used to image the beam area on the grating onto the emitting surface of $LiNbO_3$ crystal.

$LiNbO_3$ based pulse front tilting setup is one of the most intense table-top ultrafast THz sources [30]. In 2011, Hirori et al. reported single cycle THz pulse with amplitude exceeding 1 MV/cm at room temperature [31]. Due to its strong THz radiation at low THz frequency, this technique was used to generate THz wave in the THz-radiation-enhanced-emission-of-fluorescence (THz-REEF) parts which will be discussed in this review.

4) Organic crystal

Organic crystals have recently become a great interest for ultra intense THz pulse generation. In 1992, Zhang et al. first demonstrated the THz pulse generation from 4-N-methylstilbazolium tosylate (DAST) [32]. In 2011, a high quality THz beam generated from DAST with maximum electric field of 1.35 MV/cm was demonstrated [33]. However, although the THz spectrum extended up to 5 THz, a transverse optical (TO) phonon absorption of DAST can be clearly seen at 1.1 THz. To avoid this phonon absorption, other than cooling the crystal to suppress the vibration modes, alternative organic crystals such as 2- (3-(4-hydroxystyryl)-5,5-dimethylcyclohex-2-enylidene) malononitrile (OH1) and 4-N,N-dimethylamino-4′-N′-methyl-stilbazolium 2,4,6-trimethylbenzenesulfonate (DSTMS) can be used. In 2015, Shalaby and Hauri generated an extremely bright THz bullet with peak field up to 83 MV/cm [34], which holds the current record of THz generation from an EO crystal. Meanwhile, the demanding conditions for growing good organic crystals in large dimension as well as the low damage threshold of organic crystals bring challenges to their wide use as THz sources.

5) Air plasma

Other than using solid materials, such as semiconductor crystals and photoconductive antenna, the ambient air can be ionized to the form of air-plasma by intense laser beams to generate broadband coherent THz radiations. THz generation through air-plasma can be conducted with many different methods. For example, THz radiation from single-color laser beam induced plasma was first reported by Hamster et al. [35]. Later, the generation efficiency was proved to be several orders of magnitudes higher if the plasma is induced by a mixture of two-color (fundamental and the second harmonic) femtosecond laser beams [36]. The mechanism of such a strong THz generation efficiency have been explained by four-wave-mixing (FWM) model [37], and transient photocurrent model [38]. More details of THz generation from air-plasma will be reviewed in the next section.

1.2.2 Terahertz detection

There are different terahertz detection methods [17,39]. In this section, we mainly introduce THz detection methods based on electro-optical sampling. More broadband gas based THz detection methods will be introduced in the following sections.

1) Free space electro-optic sampling

The electro-optic (EO) sampling technique measures the actual electric field of a THz pulse in time domain, sensing not only the amplitude, but also the phase information with high precision [17,39]. Taking advantage of second-order nonlinear optical process the Pockels effect in EO crystals, its mechanism can be seen as the reverse phenomenon of optical rectifications.

The Pockels effect indicates that a static external electric field can induce birefringence proportional to the field amplitude in a nonlinear material. Replacing the static electric field by a relatively slowly changing THz field, the THz field variation can be detected by measuring the birefringence it induces in an EO crystal. When without a THz field, the vertically polarized optical probe pulse will not undergo any polarization change after going through the EO crystal. After passing a quarter-wave-plate and a Wollaston prism, the optical pulse polarization will first become circular and then get separated to two orthogonal components. Eventually the two photo-diodes of the balanced photo-detector that detects the difference between the two "eyes" will see same intensity in both "eyes" and return zero. When with the existence of a THz field, the birefringence it induces in the EO crystal will change the polarization of the probe pulse, therefore result in an unbalanced value proportional to the induced birefringence at the detector. With ZnTe as the detector crystal, the polarizations of the probe pulse and the THz pulse are typically set to be parallel with its [1 $\bar{1}$ 0] to give an optimum measurement [17].

The phase retardation $\Delta\phi$ experienced by the probe beam in the EO crystal can be expressed as

$$\Delta\phi = (n_y - n_x)\frac{\omega L}{c} = \frac{\omega L}{c} n_O^3 r_{41} E_{THz}, \quad (7)$$

where n_x and n_y are the refractive index along the two axises, n_O is the refractive index at the optical frequency, L is the distance the probe beam goes through inside the crystal and r_{41} is the EO efficient. The intensities of the split probe beams at the balanced photo-detector are

$$I_x = \frac{I_0}{2}(1-\sin\Delta\phi) \approx \frac{I_0}{2}(1-\Delta\phi), \quad (8)$$

$$I_y = \frac{I_0}{2}(1+\sin\Delta\phi) \approx \frac{I_0}{2}(1+\Delta\phi), \quad (9)$$

where I_0 is the incident probe beam intensity. Take the approximation that $\Delta\phi \ll 1$, the signal measured by the balanced photo-detector will be directly proportional to the THz field amplitude:

$$I_s = I_y - I_x = I_0\Delta\phi = \frac{I_0\omega L}{c} n_O^3 r_{41} E_{THz} \propto E_{THz}. \quad (10)$$

In reality, the temporal resolution or spectral bandwidth is limited by several factors, such as: the probe pulse duration, the dispersion of nonlinear susceptibility, the phase matching condition between the optical group velocity and the THz phase velocity, and the absorption of the crystal. For ZnTe, due to its TO phonon resonance at 5.3 THz, the detector response is negligible above 4 THz [17,39].

1.2.3 Terahertz time-domain techniques

1) Time-resolved pump-probe technique

As the base for THz time-domain techniques and a critical tool to study ultrafast phenomena, time-resolved pump-probe technique is taking advantage of the short and intense pulses of ultrafast lasers interacting with a material. The induced optical excitations can range from ionization, transient photo-current, birefringence to lattice vibrations, etc.

In a pump-probe set-up, the relative time delay between the pump pulse, which will create the transient excitations in the media, and the probe pulse, which is sent to probe the excitations, is fine controlled, mostly by a translational stage that changes the beam path of one of the beams. The temporal resolution of this technique is usually at the magnitude of femto-second, depending on the pump and probe pulse durations.

2) Terahertz time-domain spectroscopy

The basic methodology of THz time-domain spectroscopy (TDS) is similar to an ultra-fast pump-probe set-up [40,41]. The optical beam is split into the pump and probe beams, and the time delay is controlled by moving a translational stage. The pump beam is used to excite the THz emitter to generate THz beam. The THz beam is collected and focused onto the THz detector where the THz induced transient will be detected by the probe beam. The THz emitter and detector can be chosen among crystal, photo-conductive antenna and gas based methods, depending on the requirements of the measurements, such as THz intensity or detection bandwidth [17]. To induce spectroscopy on a sample, the TDS measurements will be made with and without the sample in the THz beam path, either in transmission mode or reflection mode. The difference between the two measurements gives not only the absorption but also the dispersion of the sample in THz frequencies by analyzing the Fourier transforms of the waveforms.

1.3 Terahertz air-photonics

1.3.1 Terahertz generation from air plasmas

1) One-color scheme

Filamentation is the process by which a high-intensity beam self-focuses through nonlinear processes and collapses. This plasma channel stabilizes the beam at vary diameters (30 to 100) and maintains high intensities over ranges much longer than the Rayleigh length of a traditional, geometrically focused beam.

Intense broadband THz generation from ionized gas drew a great amount of attention ever since it was first demonstrated by Hamster et al. in 1993 [35]. In this work, strong femtosecond laser pulses were focused into a Helium gas target, generating strong emission of THz pulses with a conversion efficiency of less than 10^{-6}. The mechanism behind the THz radiation is the Ponderomotive force at the focus of the laser beam. The Ponderomotive force is experienced by a charged particle in an inhomogeneous oscillating electro-magnetic field, pushing the particle toward the area of low optical intensity regardless of the sign of the charge [42]. However, since the ions are many orders of magnitude heavier compared to electrons, these forces generate a large density difference between ionic and electronic charges, and this charge separation results in a powerful electromagnetic transient [43].

The following relation between the emitted THz power from a one-color plasma and the excitation laser parameters was proposed by Hamster and coworkers in 1994 [44]:

$$P_{THz} \propto \left(\frac{W}{R_0}\right)^2 \frac{\lambda^4}{\tau}, \quad (11)$$

where W is the laser pulse energy, R_0 is the $1/e^2$ radius of the laser beam at the focus, λ is laser wavelength and τ is the pulse duration. Therefore, this equation predicts a strong dependence of the THz power on the wavelength and the pulse duration of the excitation laser. In the presence of strong bias field, the generation efficiency can be improved to comparable to that of THz radiation from semiconductor surface [45].

At the focus of the laser beam, the ionization front is

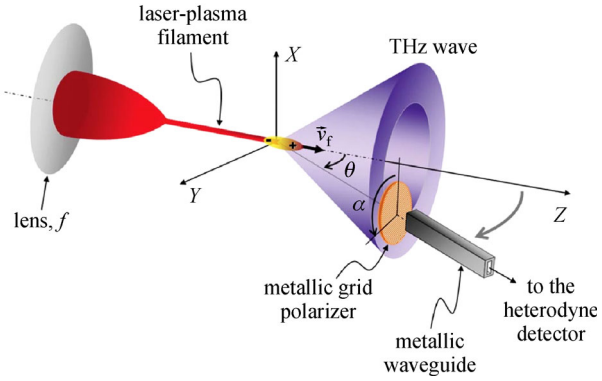

Fig. 1 Experimental setup for measuring the THz radiation pattern from a laser-induced filamentation (Reprinted from Ref. [46])

moving in the wake of the laser pulse at light velocity, therefore generates THz radiation in a Cherenkov radiation cone shape in the forward direction (Fig. 1) [46].

The angular energy density distribution of the THz radiation can actually be expressed as [47]

$$f(\omega,\theta,L) = \frac{\sin^2\theta}{(1-\cos\theta)^2}\sin^2\left(\frac{L\omega}{2c}(1-\cos\theta)\right), \qquad (12)$$

where ω is the radiated THz frequency, θ is the emission angle, L is the longitudinallength of the plasma column, and c is the speed of light. As we can see, the THz radiation angular distribution has something to do with the plasma length. To explore the extreme case of THz radiation from "microplasma", where the plasma length is at μm scale, Buccheri et al. demonstrated this fact with such a small length of plasma, the THz radiation cone angle opens up to about 80° [48].

2) Two-color scheme

All the THz generation schemes from gas plasma mentioned in last section use only one color laser pulses as the excitations. The mixing of laser pulses fundamental ω and their second harmonics (SH) 2ω to create the plasma has shown to provide enhancement of THz generation efficiency by several orders of magnitude [36].

Figure 2 illustrates a basic experimental setup for the two color air plasma generation method. The SH of the laser pulse is usually generated by using a type-I β-barium borate (BBO) crystal. The THz radiation intensity is maximized when the fundamental and SH polarizations are parallel, and is almost negligible when they are perpendicular [49–51]. THz radiation from two-color laser induced air plasma can be phenomenologically described as FWM process, which is a third order nonlinear optical process. The model can be expressed as

$$E_{\mathrm{THz}}(t) \propto \chi^{(3)} E_{2\omega}(t) E_{\omega}^{*}(t) E_{\omega}^{*}(t), \qquad (13)$$

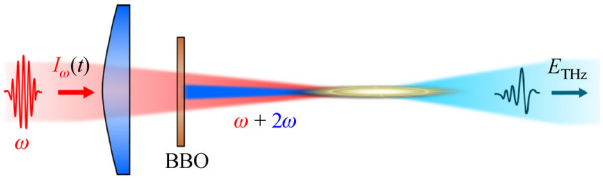

Fig. 2 Schematic demonstration of experimental setup for THz generation from two-color laser induced air plasma. An intense femto-second laser beam ω is focused by a lens to generate plasma in the air, β-BBO is used to generate 2ω

where E_{THz}, E_{ω} and $E_{2\omega}$ are respectively the THz, the fundamental and the second harmonic (SH) electric field and $\chi^{(3)}$ is an effective third-order nonlinear susceptibility of the plasma filament. This relation has been experimentally confirmed by Xie et al. in 2006 [49]. We can see that above the ionization threshold, the generated THz field is proportional to intensity of the fundamental laser and is also proportional to the square root of the second harmonic laser. Other than the ambient air, noble gases can also be used in the two-color plasma THz generation scheme. The generation efficiencies from various noble gases highly depend on their ionization potentials [52]. The strongest THz emitter among them appeared to be Xenon.

The generated THz field from two-color air plasma can be modified by changing the phase between the fundamental pulses and the SH pulses. In the FWM model, this can be expressed as

$$E_{\mathrm{THz}}(t) \propto \chi^{(3)} E_{2\omega}(t) E_{\omega}^{*}(t) E_{\omega}^{*}(t) \cos\varphi, \qquad (14)$$

where φ denotes the phase difference between ω and 2ω. Due to the dispersion of the two colors in air, the phase shift between these two color beams varies as they propagate. Therefore, the phase φ can be easily controlled by shifting the β-BBO longitudinally [50]. However, due to the laser intensity change toward the focus and the spatial limit between the focusing optic and the focus, simply shifting the β-BBO cannot control the phase φ precisely or significantly enough for certain purposes, such as remote generation of THz [53]. In those cases, phase compensators including a pair of silica wedges were exploited in order to fine tune the phases and polarizations of the ω and 2ω beams [54]. Figure 3 lists two types of phase compensators, which respectively control the two color beams in one beam path or in two separate paths. With the help of phase compensator, the generated THz field strength as well as the pulse polarity can be modified explicitly [53]. Further examination on how the various pump pulse polarizations affect the THz generation field was also enabled due to the phase compensator technique [54].

Although many experiments support the FWM model as the principle mechanism for THz generation from two-color laser induced air-plasma, the third order nonlinearity

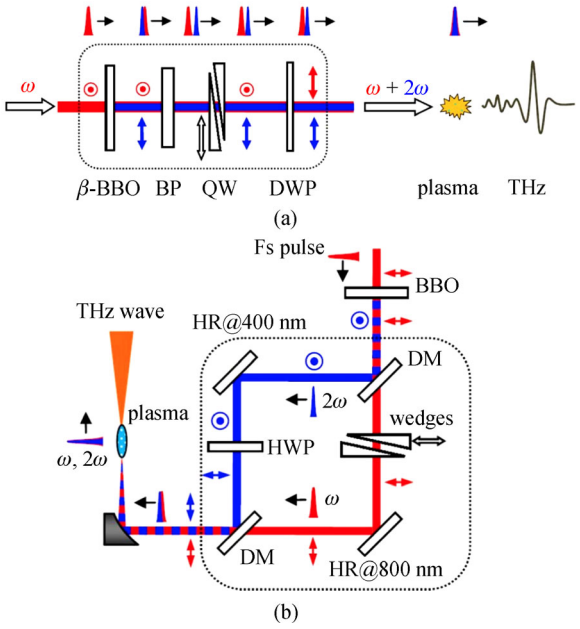

Fig. 3 (a) Inside the dashed line is the in-line PC (phase compensator). (b) Schematic illustration of the PC incorporated with a wedge pair: DM used to separate or recombine ω and 2ω beams; HWP used to control the polarization of the 2ω beam. DWP, dual-wavelength waveplate; BP, birefringent plate (α-BBO); QW, quartz wedges; Fs, femtosecond; HR, highly reflect; DM, dichroic mirror (Reprinted from Ref. [53] ©2011 IEEE)

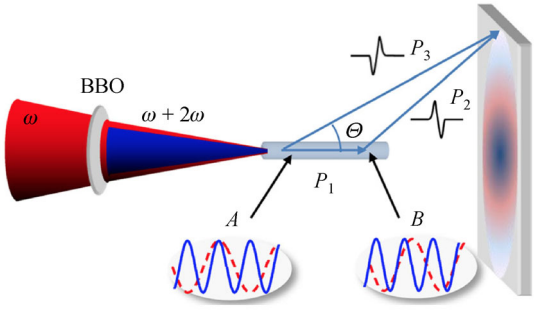

Fig. 4 Schematic of THz emission from a long, two-color laser-induced filament. The phase difference between 800 nm (dashed red curves) and 400 nm (solid blue curves) pulses along the filament results in a periodic oscillation of microscopic current amplitude and polarity. The resulting far-field THz radiation is determined by interference between the waves emitted from the local sources along the filament. P_1, P_2 and P_3 are respectively the optical path along the different directions as shown in the figure, θ is the angle between P_3 and P_1 (Reprinted from Ref. [57])

susceptibility $\chi^{(3)}$ of bound or free electrons is too small to explain the high intensity of THz radiation. Therefore, a transient photocurrent model was developed to explain coherent terahertz emission from air excited by a symmetry broken laser field composed of ω and 2ω laser pulses [38,55]. In this model, a nonvanishing transverse plasma current is produced when the bound electrons are stripped off the ions by an asymmetric laser field, e.g., a mixture of two-color laser field with a proper relative phase. This photocurrent transient, occurring on the timescale of the photoionization, can thus produce electromagnetic radiation at THz frequencies. The electron dynamics right after the ionization were treated classically by Kim et al. [38,55], whereas a full quantum mechanical simulation was reported by Karpowicz and Zhang [56].

For elongated two-color filamentation, the THz radiation forms a cone shape due to off-axis phase matching [57]. The THz yield and angular distribution depend highly on the filament dimensions, and the dephasing length l_d over which the THz radiation polarity remains the same. l_d can be expressed as

$$l_d = \left(\frac{\lambda}{2}\right)(n_\omega - n_{2\omega})^{-1}, \quad (15)$$

where λ is the wavelength at ω, n_ω and $n_{2\omega}$ are respectively the refractiveindex at frequency ω and 2ω. For filament with electron density of 10^{16} cm^{-3} inambientair, the dephasing length is about 22 mm.

For a filament comparable to or shorter than the dephasing length, THz waves generated along the filament have both positive polarity and negative polarity (As shown in Fig. 4) [57]. Those components interfere with each other constructively or destructively in the far field, depending on their path difference which is related to the radiation angle, forming a donut shape far field radiation profile. The angle of the THz radiation cone depends on the plasma length [58]. The longer the focal length of the focusing lens used for plasma generation is, the longer the plasma is, and the smaller the THz radiation cone is.

You et al. also found out that the generation yield increases almost linearly with the plasma filament length, so one can increase the THz generation by simply extending the plasma length [57]. Recently, different methods to tailor the filamentation toward more intense THz generation have been reported, including concatenating two plasmas into one [59].

1.3.2 Terahertz detection by air-plasmas

Other than being an efficient emitter for THz radiation, gas plasmas can also be used as THz wave sensors. The related techniques include THz-air-biased-coherent-detection (ABCD) [53], THz-radiation-enhanced-emission-of-fluorescence (REEF) [60,61], and THz-enhanced-acoustic (TEA) [62]. THz-ABCD technique is impressive for its extraordinary capability of super broadband coherent THz wave sensing, with the assistance of electrodes as the local oscillator. Circumventing the limitation of the needs of a local oscillator, The THz-REEF technique features great potential in THz remote sensing.

1) Terahertz-air-biased-coherent-detection

As we have observed in the cases of EO sampling of THz waveform versus optical rectification THz generation, a reversed version of THz generation process can often be utilized to detect THz wave. Similarly, the two-color laser induced air plasma THz generation has a counter-part in detection as well. In the FWM model, if we replace the $E_{2\omega}(t)$ in the right hand side of Eq. (13), there will actually be a 2ω light generation that's proportional to THz field:

$$E_{2\omega}^{\mathrm{THz}} \propto \chi^{(3)} E_{\omega} E_{\omega} E_{\mathrm{THz}}, \tag{16}$$

where $E_{2\omega}^{\mathrm{THz}}$, E_{ω} and E_{THz} are the electric field amplitudes of the 2ω, ω and THz waved respectively and $\chi^{(3)}$ is the third-order susceptibility of the gas. This third order nonlinear process was known as THz-field-induced-second-harmonic (TFISH) [63]. Since the second harmonic can only be directly detected by its optical intensity, without a local oscillator, the measured signal is proportional to the THz radiation intensity, i.e., $I_{2\omega}^{\mathrm{THz}} \propto I_{\mathrm{THz}}$. The phase information of the THz wave is lost in this measurement, therefore, it is incoherent detection.

However, when a second harmonic local oscillator $E_{2\omega}^{\mathrm{LO}}$ is introduced, its cross term with $E_{2\omega}^{\mathrm{THz}}$ will be generated for coherent THz detection. The total second harmonic intensity can be expressed as

$$\begin{aligned} I_{2\omega} &\propto \langle E_{2\omega}^{2} \rangle = \langle (E_{2\omega}^{\mathrm{THz}} + E_{2\omega}^{\mathrm{LO}})^{2} \rangle \\ &= \langle E_{2\omega}^{\mathrm{THz}^2} \rangle + 2\langle E_{2\omega}^{\mathrm{THz}} E_{2\omega}^{\mathrm{LO}} \rangle + \langle E_{2\omega}^{\mathrm{LO}^2} \rangle. \end{aligned} \tag{17}$$

The extraction of the cross term $2\langle E_{2\omega}^{\mathrm{THz}} E_{2\omega}^{\mathrm{LO}} \rangle$ from the above equation is essential for coherent THz detection. In the original demonstration of broadband THz wave detection with laser-induced plasma in gaseous media by Dai et al. in 2006 [64], the cross term was extracted through making it dominant by a strong intensity. When $E_{2\omega}^{\mathrm{LO}} \gg E_{2\omega}^{\mathrm{THz}}$, the term $E_{2\omega}^{\mathrm{THz}^2}$ can be ignored, and the term $E_{2\omega}^{\mathrm{LO}^2}$ is a DC term that can be filtered out through a lock-in amplifier or modulating the THz wave. However, since the local oscillator $E_{2\omega}^{\mathrm{THz}}$ (400 nm) was contributed by the white light generation, this technique requires very high probe pulse energy. In the case of Ref. [65], when the probe pulse energy is higher than 440 μJ, the coherentdetection eventually dominates. At this point, the detection technique was named THz-air-breakdown-coherent-detection.

To reduce the probe pulse energy requirement and increase the signal noise-ratio of the air-based coherent THz detection, an external ac bias across the focal point of the probe beam was applied to provide a local oscillator for the second harmonic generation (Fig. 5) [66]. Using lock-in amplifier to lock onto the ac bias frequency would help successfully extract the coherent detection cross term in Eq. (17). With this technique, only 100 μJ probe pulse energy was typically needed, and due to the heterodyne detection nature, the signal-noise-ratio was significantly improved. The air-based detection technique's name was therefore switched to THz-air-biased-coherent-detection to accentuate the use of ac bias, but the acronym THz-ABCD still stands.

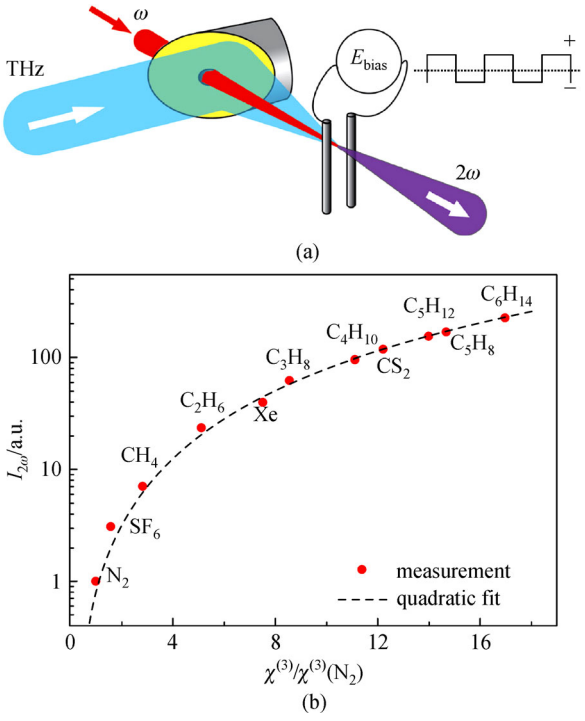

Fig. 5 (a) Basic concept of THz-ABCD: electrodes are placed at the geometric focus of collinearly focused THz and optical probe beams with a variable time delay. Second harmonic light is induced from the THz field and the local bias field E_{bias}. Modulating E_{bias} allows for heterodyne detection for enhanced sensitivity. (b) Measured second harmonic intensity vs third order nonlinear susceptibility $\chi^{(3)}$. All $\chi^{(3)}$ are normalized with respect to nitrogen (Reprinted from Ref. [66] ©2011 IEEE)

The detected second harmonic intensity is a function of normalized third order nonlinear susceptibility $\chi^{(3)}$ along with a quadratic fit [67]. C_6H_{14} provides more than 243 times the sensitivity compared with N_2 or air. Using gases with larger $\chi^{(3)}$ and higher probe pulse energy can help to optimizethe sensitivity of the air-plasma detector.

Due to the gaseous media used for detection, one of the most important features of THz-ABCD is that its detection bandwidth is only limited by the probe pulse duration [68,69]. With a sub-35 femtosecond laser pulse, the THz-ABCD bandwidth can reach 30 THz [53].

1.3.3 Terahertz remote sensing technology using terahertz air-photonics

To prevent the THz wave from traveling remotely which

would result in substantial absorption by the water vapor in the atmosphere [41,70], we have proposed a THz remote sensing scheme in Ref. [71] (Fig. 6). In this scheme, one branch of laser beam is focused remotely to generate THz wave near the target, whereas another branch of laser beam is also focused remotely in order to detect THz wave that has been reflected back from the target with the spectroscopic information encoded. The spectroscopic information is eventually picked up by the fluorescence radiation of the plasma, and is detected remotely with photo multiplier tube (PMT). In this proposed method, the beams that have to travel the distance for remote sensing are the infrared (IR) optical beams, their second harmonics, and the fluorescence radiation at UV frequency range. It successfully avoids the situation where THz wave has to travel along distance.

Among the techniques that constitute this envisioned scheme, many have already been experimentally proved feasible in the laboratory. For example, a proof-of-concept "all air-plasma" THz spectroscopy system was demonstrated in 2011 without the need of solid-state materials [72]. Standoff THz generation by sending optical beam up to 30 m has also been reported in the same year [37]. However, before this envisioned scheme can be utilized in the field, many problems still need to be overcome. For instance, sending a tunable and robust optical beam far away to generate intense THz radiation with the real life perturbations from the atmosphere is challenging. In addition, whether it is possible to sense THz coherently when the THz beam and the optical probe beam are not traveling collinearly is still uncertain. The research of this draft is set to further investigate these issues.

1.4 Ring-Airy beams

1.4.1 Airy beam family

Finding a localized non-spreading or non-diffracting wave function has been a great interest of scientists in optics or atom physics. In 1979, Berry et al. have shown in the context of quantum mechanics that for an Airy wave packet its probability density propagates in free space without distortion [73]. It was noted that in one dimension, the Airy packet is the only nontrivial solution (apart from a plane wave) that remains invariant with time [74].

The similarity between the potential free Schrödinger equation and the paraxial diffraction equation bridges the difference between optics and quantum mechanics and made optics a field very friendly for experimental demonstration of localized non-spreading waves [75]. In 1987, Durnin et al. first theoretically proposed and then experimentally demonstrated one of the most well-known 2D diffraction-free optical waves, Bessel beam [76,77]. Their work inspired many other interesting discoveries of non-diffracting beams, including further study on Bessel beams [78], Mathieu beams [79], and Ince-Gaussian beams [80], etc.

However, all of the solutions above are known to convey infinite power, whereas in reality, those beams have to be truncated by a finite aperture in order to be generated. In early 2007, the truncated version of 1D and 2D Airy beams was first studied theoretically [81]. The special acceleration dynamics and quasi-diffraction-free properties were demonstrated with a simulation developed from paraxial diffraction equation

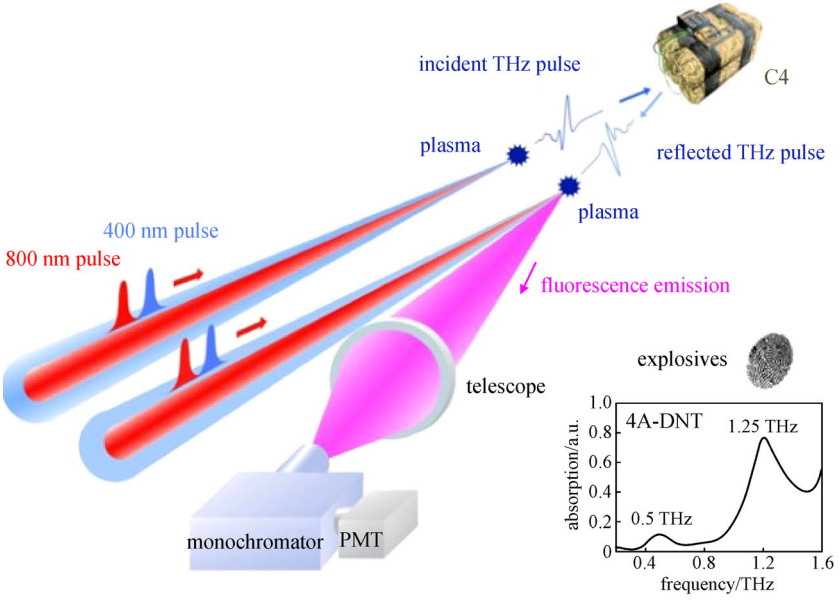

Fig. 6 Envisioned scheme for THz stand-off generation and detection. Two dual-color pulses are focused close to the target under investigation creating a plasma emitter and a plasma sensor. Inset shows an absorbance spectrum of 4A-DNT retrieved through THz-REEF (Reprinted from Ref. [71])

$$i\frac{\partial\phi}{\partial\xi}+\frac{1}{2}\frac{\partial^2\phi}{\partial s^2}=0, \tag{18}$$

where ϕ is the electric field envelope, $s=x/x_0$ is a dimensionless transverse coordinate with x_0 as an arbitrary transverse scale, $\xi=z/kx_0^2$ is the normalized propagation distance with respect to the Rayleigh range, andk is the wavenumber.

With an initial condition

$$\phi(s,\xi=0)=Ai(s)\exp(as),\ a>0, \tag{19}$$

where $Ai(\cdot)$ is the Airy function, and the decay factor a (>0) is added to give a finite Airy tail, Eq. (18) can be solved [81].

The results can be generally extended to two dimensions (2D) as well, in the form

$$\phi=Ai\left(\frac{x}{x_0}\right)Ai\left(\frac{y}{y_0}\right)\times\exp\left(\frac{x}{\omega_1}\right)\exp\left(\frac{y}{\omega_2}\right), \tag{20}$$

where $Ai(\cdot)$ is the Airy function, x_0 and y_0 are arbitrary transverse scales in x and y directions respectively, and ω_1 and ω_2 are exponential decay factors in x and y dimensions respectively.

Later in 2007, the same group has experimentally demonstrated the Airy beams in both 1D and 2D [82]. To generate Airy beams, computer controlled liquid crystal spatial light modulator (SLM) was used to impose a cubic-phase modulation with phase masks for 1D and 2D. Experimental results proved both their the ability to remain diffraction-free over long distances while they tend to freely accelerate during propagation [81].

Several years later, Abdollahpour et al. demonstrated the realization of Airy-Airy-Airy (Airy^3) light bullet by combining spatial 2D Airy beam with a temporal Airy pulse shape [83]. The temporal Airy profile was obtained by imposing a cubic spectral phase on an initial 35 fs Gaussian laser pulse with the use of a grating-telescope compressor [84].

1.4.2 Ring-Airy beams

After the introduction of 1D and 2D Airy beams, the study of Airy beams family has then been extended to the radially symmetric Airy beam [82,85,86]. Its distribution is described by

$$u_{\rm o}(r,0)=Ai\left(\frac{r_{\rm o}-r}{\omega}\right)\exp\left[a\left(\frac{r_{\rm o}-r}{\omega}\right)\right], \tag{21}$$

where $Ai(\cdot)$ is the Airy function, r is the radius, $r_{\rm o}$ is the primary ring radius, w is a scaling factor and α is a decay factor.

With the help of a phase mask the radially Airy distribution can be generated, featuring the distinctive ring structures. Therefore, the beam is also referred to as "ring-Airy" beam [85].

The intensity contrast $I(z)/I(0)$ of a ring-Airy beam as a function of the propagation distance, where I is the peak intensity of the beam at a certain propagation distance [85]. As the beam propagates, the primary ring is accelerating toward the optical axis in a parabolic trajectory, similar as what we have seen in 1D and 2D cases [82]. Research result shows that the ring-Airy beam has an auto-focusing nature. Also, the intensity contrast of the beam before the focus is very low, while at focus it reaches ~195. Compared to an equivalent Gaussian beam that is focused by a lens with the same effective focal length, the contrast can be enhanced up to twice. The effective f-number of a ring-Airy beam can be expressed as

$$(\#F)_{Ai}\approx f_{Ai}/4R(0), \tag{22}$$

where f_{Ai} is the effective focal length of an auto-focusing ring-Airy beam, $R(0)$ is the initial radius of the primary ring. Whereas the f-number of a Gaussian beam with the same initial waist $\omega_G=R(0)$ focused by a lens with the same focallength $f_G=f_{Ai}$ is

$$(\#F)_G\approx f_{AG}/2R(0). \tag{23}$$

As we can see, with the same initial beam size, a ring-Airy beam can reach an effective f-number twice smaller than that of a Gaussian beam, giving an insight to the abrupt increase of its intensity at focus.

1.4.3 Generation of ring-Airy beams

1) Fourier transform approach

In the first demonstration of ring-Airy beam [85], the Fourier transform of the beam distribution was first encoded onto a phase filter and applied onto a phase only reflective SLM. The phase modulation capability of the device is up to 2π so phase wrapping has to be used for any phase change higher than 2π. Then the phase-modulated beam will be Fourier transformed by a lens. An opaque mask was used to block the unwanted zero-order. The schematic demonstration and the phase mask [87].

2) Direct phase approach

In 2011, Chremmos et al. have proposed a method to create a family of abruptly auto-focusing beam [88], with the form of

$$u(r,0)=A(r)\sin\Big(\phi(r)\Big),$$

$$\phi(r)=\begin{cases}C\cdot(r-r_{\rm o})^{3/2},\ \forall r\geqslant r_{\rm o},\\ 0,\ \forall r<r_{\rm o},\end{cases} \tag{24}$$

where A is an envelope function such that the total energy

is finite, ϕ is the phase of a sub-linear chirp, $C>0$ is a constant, $1<\beta<2$ is the index of the chirp. When $\beta=3/2$, the generated beam will auto-focus with a parabolic caustic.Therefore it is effectively equivalent to a ring-Airy beam.

To realize this pre-engineered auto-focusing beam, the sinusoidal term can be expressed by the Euler's formula:

$$\sin\Big(\phi(r)\Big)=\frac{1}{2\mathrm{i}}\Big(\mathrm{e}^{\mathrm{i}\phi(r)}-\mathrm{e}^{-\mathrm{i}\phi(r)}\Big), \tag{25}$$

where the first term denotes the outward wave and second the inward wave. Since we only care about the interference effect of the wave that will naturally come inward of the Airy primary ring structure, we can keep only the inward wave term, and reach to a math description that require only phase control:

$$u(r,0)=A(r)\mathrm{e}^{\phi(r)},$$

$$\phi(r)=\begin{cases} C\cdot(r-r_{\mathrm{o}})^{3/2},\ \forall r\geqslant r_{\mathrm{o}}, \\ 0,\ \forall r<r_{\mathrm{o}}. \end{cases} \tag{26}$$

With such a method without Fourier transform, the loss due to the undesired zero order is reduced from ~90% for the Fourier transform approach to ~15% for the direct phase approach. The energy efficiency of the method allows the work in next section where high intensity beam is needed in order to generate plasma. Another advantage of the direct phase method would be the flexibility of changing the auto-focusing caustic by changing the index β. For example, when β = 3/2, the generated beam is equivalent to ring-Airy beam with a parabolic caustic; when β = 1, the generated beam is equivalent to Bessel beam; when β = 2, it is equivalent to a typical focusing scenario.

3) Second-harmonics generation of ring-Airy beams

During the experiments of using a ring-Airy beam to generate two color laser induced plasma as THz source in 2015, the second harmonic generation (SHG) from the ring-Airy beam using β-BBO was observed to preserve the auto-focusing property and the focus will spatially overlap with the focus of the fundamental beam [89]. However, since the scope of the work mainly focused on THz generation from the plasma, the propagation property of the second harmonic (SH) beams was not explored with detail. In a recent report by Koulouklidis et al., it has been demonstrated both theoretically and experimentally the SHG from ring-Airy beams would preserve the phase distribution of the fundamental harmonic (FH) ring-Airy beam [90]. Therefore the SH will maintain the auto-focusing property with a focus position coincide with the FH beam focus [90].

Surprisingly, even after focusing with a lens the SH and FH still spatially overlap over an elongated focal volume. Both FH and SH show two foci as predicted by the case of all Janos waves [91]. However, the SH beam also shows one extra intense focus at the center, approximately at the focal point of the lens, due to the focusing of the pedestal term of the SH that does not have any autofocusing behavior.

The phenomena match very well with what have been observed during the work on THz generation from two-color ring-Airy beam induced plasma [89], as mentioned in the next section.

1.4.4 Nonlinear propagation of ring-Airy beams in air

In 2013, Panagiotopoulos et al. have first demonstrated ring-Airy beam propagation in a nonlinear regime [92]. Low and high order nonlinear optical effects, including the Kerr effect, multi-photon absorption and ionization were observed when intense ring-Airy beam is propagating in silica. Due to the high energy loss of Fourier transform approach for ring-Airy beam generation, a microscope objective has to be used to create beam intensity high enough to cause nonlinear effects in silica.

Ring-Airy beam nonlinear propagation is demonstrated in ambient air. Thanks to the direct phase generation approach, intense ring-Airy laser pulses with 35 fs pulse duration and pulse energy up to 0.65 mJ were generated. A relative low repetition rate of 50 Hz was chosen to reduce the thermal damage on the SLM without sacrificing the pulse energy. Although the beams possess the auto-focusing properties by themselves, further focusing with 100 mm focal length lens was used to help generate the plasma.

The induced plasmas were recorded using a linear scaling CCD and imaging optics, as shown in Fig. 7(a).

Since the fluorescence image on the CCD sensor is actually an Abel transform of a radially symmetric fluorescence emission from the focal volume, by applying inverse Abel transform on the images we can accurately estimate the radial distribution of the fluorescence emission $F(r,z)$ [92]. The fluorescence distribution emission $F(r,z)$ for various input optical energies are shown in Fig. 7(b).

In the figure, from top to bottom, the plasma images are respectively formed by focusing a ring-Airy beam with 0.25, 0.35, 0.45, 0.55 and 0.65 mJ pulse energy. It is clearly observed that the peak intensity of the plasma string shifts as the input energy increases, as a characteristic feature of ring-Airy beams [92]. When we compare the plasmas induced by ring-Airy and Gaussian beams (bottom trace in Fig. 7(b)), we notice that the ring-Airy beam induced plasma is significantly longer in contrast to the Gaussian plasma. This phenomenon is proved by recent work of Koulouklidis et al., as mentioned in last section [90]. The report has shown experimentally when focusing a ring-Airy beam, the focal volume appears to be elongated due to the dual foci property of Janos beam [91]. Also observable

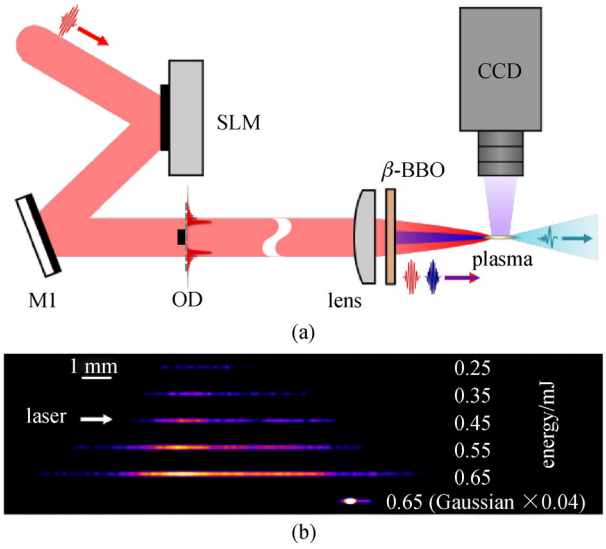

Fig. 7 (a) Experimental set-up for observing the ring-Airy beam induced air plasma; (b) fluorescence false color images of ring-Airy beam plasmas (top 5) with pulse energy from 0.25 to 0.65 mJ, and Gaussian beam plasma (bottom) with pulse energy 0.65 mJ. The Gaussian plasma image intensity has been reduced 25 times to reach similar visibility of the ring-Airy beam plasmas

is the emergence of the low-intensity secondary peaks following the primary focus, which could be qualitatively explained by the combination of two foci of the FH ring-Airy beam and the intense center focus of the SH beam due to its pedestal term.

Not only the length difference is apparent, but the difference in fluorescence emission intensity between the ring-Airy plasma and Gaussian plasma is also obvious. For example, with 0.65 mJ pump pulse energy, the maximum recorded fluorescence intensity of the Gaussian plasma is 210 times brighter than that of plasma generated by the ring-Airy beam. Furthermore, as seen in Fig. 7(b), there exists a prominent focus shift between the two types of beams. With the focusing action of the lens, the ring-Airy beam preserves its autofocusing following a parabolic trajectory [90], whereas the Gaussian beam follows a linear trajectory.

2 Terahertz generation from ring-Airy beam induced plasmas

2.1 Brief introduction

Since the first demonstrations of 1D and 2D accelerating Airy beams [82], studies on the family of Airy beams started to draw great amount of attention in the nonlinear optics community. Shortly after the prediction of the radially symmetric Airy beam (ring-Airy) in 2010 [86], its unusual properties, such as the ability to autofocus with a parabolic trajectory and to abruptly increase the maximum intensity at the focus by orders of magnitude, were experimentally observed [85]. At the same time, a new family of (2 + 1)D abruptly auto-focusing (AAF) beams with pre-engineered arbitrary focusing caustics was introduced by Chremmos et al. [88]. Wide range of possible applications, such as medical laser treatment, microparticle trapping, temporal cloaking, were discussed in numerous reports.

The nonlinear propagations of novel beams other than Gaussian is always an area of interest for filamentation researchers [93–95]. One of the many promising applications of air-plasma is to serve as intense broadband table-top THz source [35,36]. Using different plasma parameters to improve the generation efficiency is a new area of interest in numerous research groups [49,96]. Among those efforts, some have tried tailoring the plasma in different ways, such as creating plasma with a gradient distribution [97], concatenating two plasmas into one [59], and putting two filaments side-by-side [98]. They have found that with those methods, they can achieve either enhancement or control of the THz radiation from the tailored two-color air-plasmas.

The characteristics of THz radiation from two-color ring-Airy beam induced air-plasma are investigated [89]. Due to the much higher generation efficiency, the study has mainly focused on two-color case instead of one-color case. Ring Airy beams' high level of tunability [88], wavepacket stability in the nonlinear regime [92], and robustness when propagating in turbulent media [99], make the plasmas induced by these novel wavepackets a promising broadband THz source for THz remote sensing and spectroscopy [53,61], a critical topic for homeland security and environmental monitoring.

2.2 Experimental set-up

The measurements to investigate ring-Airy beam induced plasma as a THz source exploited a pump-probe THz time-resolved detection system, shown in Fig. 8.The ring-Airy beams were generated by sending 35 fs, 50 Hz, 800 nm Ti-Sapphire laser pulses to a spatial light modulator (SLM, Hamamatsu LCOS-X10468-2), with a phase mask exerted. Following a similar approach to Chremmos et al. [88], the phase mask consisted of a radially chirped phase distribution

$$\phi(r) = \begin{cases} C\cdot(r-r_{\rm o})^{3/2}, & \forall r \geqslant r_{\rm o}, \\ 0, & \forall r < r_{\rm o}, \end{cases} \tag{27}$$

where r is the radius, $r_{\rm o}$ is a reference radius and C is a constant. By blocking the central part of the phase modulated Gaussian beam with an opaque disk, after some free propagation, a ring-Airy distribution was formed [88]. This method is energetically advantageous compared to a Fourier transform approach [85], since the loss of large

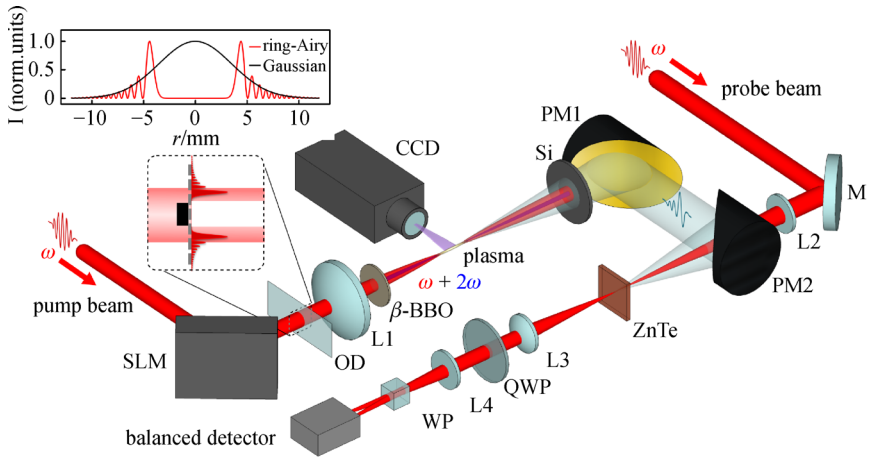

Fig. 8 Experimental set-up. SLM: spatial light modulator, OD: opaque disk, on a transparent glass slide, L: lens, PM: parabolic mirror, M: mirror. Inset: Schematic comparison between the radial intensity distribution of the ring-Airy and the Gaussian beam; zoom-in on the beam area prior and post to the glass slide: case 1 is when using the Gaussian beam, the glass slide is shifted so the OD is removed from the beam path, case 2 is when using the ring-Airy beam, the OD is moved back into the center of the beam to block the unwanted part

amount of energy in the zero-order was avoided. The Gaussian beams were generated by sending the same laser pulses to the SLM with a plain phase mask. When using the Gaussian beam, the opaque disk was removed from the beam path, as shown in the zoom-in parts of Fig. 8.

The experimental setup was designed to compare the THz radiations from air plasmas induced by ring-Airy beams and Gaussian beams. To increase the intensity enough to generate plasma in air and to precisely position the plasma, in both cases the pump beam was focused by a 100 mm focal length lens, as shown in Fig. 8. The focused ring-Airy pump beam preserves its properties, such as the abrupt focusing, except that now the focus is more intense and is shifted toward the laser source. A 50-μm-thick β-BBO was put between the lens and the plasma in order to create the second harmonic (SH) generation of the pump pulse. The SH of ring-Airy beam retains its abrupt autofocusing characteristic sharing the same acceleration to the fundamental harmonic (FH) [100]. Interestingly, the abrupt autofocusing foci of the fundamental ring-Airy and its SH overlap in space. The detailed descriptions of lens-focused ring-Airy beam and the properties of its second harmonics are addressed in last section [90,91]. The pulse energy of the pump beam before the β-BBO ranged from 0.1 to 0.65 mJ. The maximum energy that could be applied was limited by the onset of white light generation in the lens that would cause damage. Free space electro-optic sampling with a 3-mm-thick ⟨110⟩ cut ZnTe was used to detect THz waveforms [39]. A pair of off-axis-parabolic-mirrors was used to collect, collimate, and refocus the forward THz radiation from the plasma. Fluorescence images of the generated plasmas were recorded using a linear CCD camera and imaging optics.

2.3 Terahertz radiation from two-color ring-Airy beam induced plasmas

Figures 9(a) and 9(b) show the THz waveform and its spectrum generated by a ring-Airy beam induced plasma. The signal was optimized through tuning the relative phase and intensity proportion between the FH 800 nm and the SH 400 nm by adjusting the position and angle of the β-BBO crystal. The spectral bandwidth of the detected THz signal is essentially limited by the phonon absorption of the ZnTe crystal.

Because the ring-Airy air-plasma THz source under study shares the same asymmetrical laser field and interaction material with the familiar Gaussian air plasma THz source, a THz emission process similar to that of a Gaussian source is expected. To confirm this expectation, we measured the THz peak amplitude as a function of the relative phase between the two colors by scanning the β-BBO between the focus and the lens. The scanning range of the crystal was limited by the focal length of the lens and the damage threshold of the BBO. The results are shown in Fig. 10. The THz yield modulation is due to the variation of the relative phase between the two colors. The insets give examples of how the relative phase controls the THz radiation waveform polarity. Also shown in Fig. 10, these data can be fitted using the FWM model [101] at the same time of taking into account how the second harmonic generation efficiency would change as the β-BBO crystal moves closer to the plasma due to the beam intensity change on the crystal. The resulted fitting parameters give a THz yield modulation oscillation period that is consistent with the known dispersion in air [38]. We start with a FWM model expression:

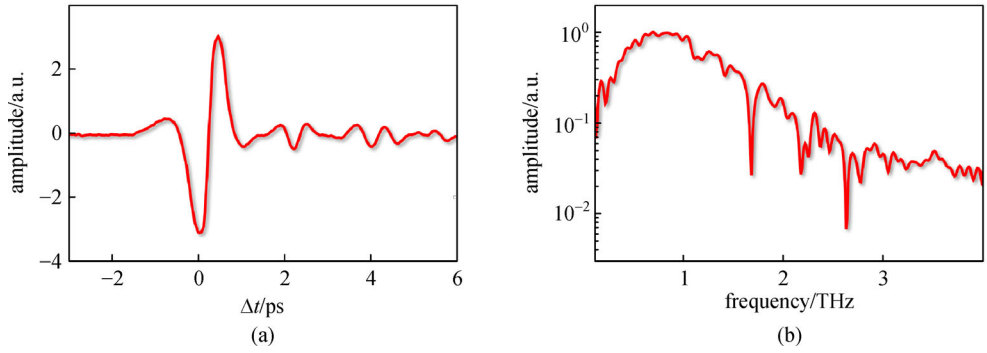

Fig. 9 (a) Typical THz waveform generated from the ring-Airy beam induced plasma pumped with a pulse energy of 0.65 mJ; (b) corresponding spectrum

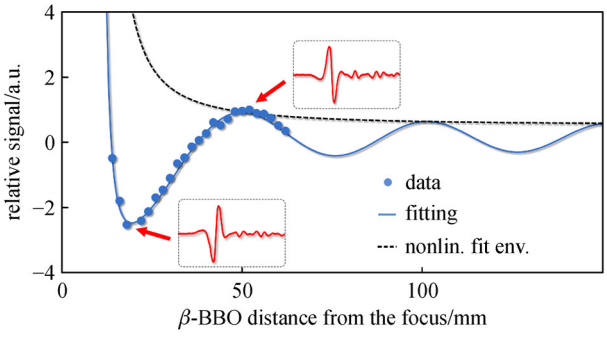

Fig. 10 THz emission peak amplitude versus the β-BBO distance from the focus. Blue dots: experimental data; blue solid curve: FWM model fitting result; black dashed curve: nonlinear fitting envelope taking into account the SHG efficiency change as the BBO is moving toward the focus; the insets show two sample THz waveforms having opposite polarities

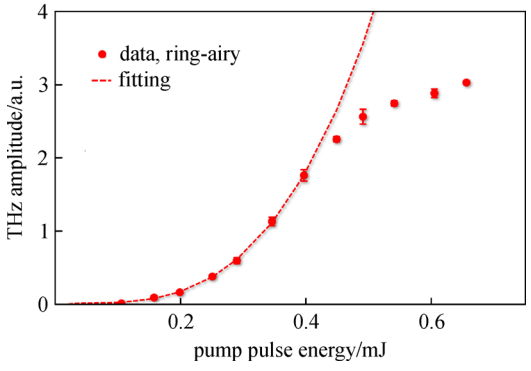

Fig. 11 Emitted THz wave peak amplitude as a function of total pump pulse energy (800 and 400 nm). Red dots: experimental data from ring-Airy beam; red dashed line: fitting of the ring-Airy data with the FWM model. The error bars are the measurements standard deviation of each point

$$E_{\mathrm{THz}} \propto a\chi^{(3)} I(I - bI^2), \tag{28}$$

where E_{THz} is the emitted THz field amplitude, a and b are constant, I is the totalbeam intensity before the BBO crystal, $\chi^{(3)}$ is the 3rd order susceptibility of air. We use the approximation that $I \propto \frac{P}{r}$ instead of $I \propto \frac{P}{r^2}$, where P is the input beampower and the primary ring radius, because most of the energy is distributed on the primary ring of the ring-Airy beam instead of the full area inside the ring. Another assumption we take is that within the scanning range, the ring-Airy beam caustic is approximately linear. Through derivation, the expression above can be transformed to another equation describing the relation between the E_{THz} and the distance z from the focus to the BBO crystal:

$$E_{\mathrm{THz}} \propto A \cdot P^2 z^{-\frac{1}{2}} + B \cdot P^3 z^{-\frac{3}{2}}, \tag{29}$$

where A and B are constants. Using this expression as a nonlinear fitting envelope (red dashed line in Fig. 11), multiplied with a sinusoidal function, we are able to fit the experimental data very well.

Figure 11 shows the emitted THz amplitude as a function of the input pulse energy. The red dots are the experimental data from the ring-Airy beam plasma, which can be fitted with the FWM model, using Eq. (28). The fitting result shows that the experimental data starts to deviate from the fitting curve at around 0.45 mJ and the deviation becomes prominent at 0.55 mJ. This implies that for higher pulse energies one should consider the photocurrent model and the intensity clamping in the filaments [102,103]. There could also be contribution from the nonlinear interaction between the beam and the lens that can cost some of the energy. When the input pulse energy is high, some energy hot spots observed on the primary ring of the ring-Airy beam tend to cause white light generation from the lens.

2.4 Comparison between ring-Airy beams and Gaussian beams

To better characterize the ring-Airy beam plasma as a THz source, we compare its THz emission with the one from a Gaussian beam induced plasma under the same experimental conditions. Figure 12(a) shows the images of the

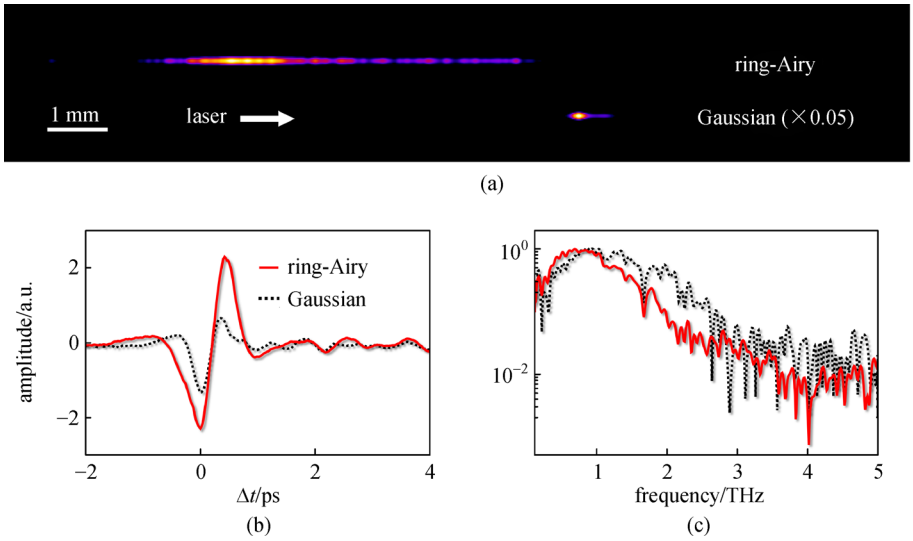

Fig. 12 (a) Fluorescence image comparison between an ring-Airy beam plasma and a Gaussian plasma (intensity reduced by 20 times), both generated with pump pulse energy 0.5 mJ; (b) measured THz waveforms and (c) their corresponding normalized spectra generated by the two plasmas in (a)

plasmas being discussed below. With a 0.5 mJ input pulse energy, the ring-Airy beam plasma THz waveform measured is shown in Fig. 12(b), whereas the one from the Gaussian beam has noticeably less amplitude. If we calculate the pulse energy by integrating the square of THz field, the THz pulse energy from the ring-Airy plasma is about 5.3 times larger than that from the Gaussian plasma. The obvious THz yield difference can be explained by the significant plasma length difference [57], as we have qualitatively verified with the interference model (see next section for detailed explanations) [104]. Both plasmas have not reached the typical air filamentation dephasing length. If we consider the possibility that a shorter plasma may emit THz with a larger angle (as shown in Fig. 13) [58], which means the THz radiation from the Gaussian beam plasma could eventually be focused tighter than that from the ring-Airy plasma, the real THz yield difference between the two might be substantially bigger than what we measured. Figure 12(c) shows the normalized spectra of the waveforms. The ring-Airy plasma THz emission has a central frequency slightly lower than the Gaussian one, which denotes that the ring-Airy plasma has a lower plasma density [38].

During the experiment, the lens location was always optimized for each measurement to avoid the signal discrepancy caused by focus location changes. Moreover, a 2-inch (50.8 mm) diameter parabolic mirror with 3-inch (76.2 mm) focal length was put after the plasma to collect the THz radiation, providing an 18.4° collecting angle, sufficient to cover the emission cone (10°) from a two-color air-plasma generated by 100 mm focal length lens [58].

In Fig. 13, the pump pulse energy dependent THz emission peak field amplitude data from the ring-Airy beam induced plasma (red dots) is plotted against the one from the Gaussian beam induced plasma (black squares). Due to the saturation effect observed in Fig. 11, in the comparison, the THz emission enhancement effect starts to reduce at large pump pulse energies. This may imply that at the same focusing condition, the THz generation saturation threshold of the ring-Airy beam induced plasma is lower than the Gaussian plasma, possibly due to the easier onset of intensity clamping effects in plasmas and nonlinear interaction with lenses by the special intensity structure of ring-Airy beams.

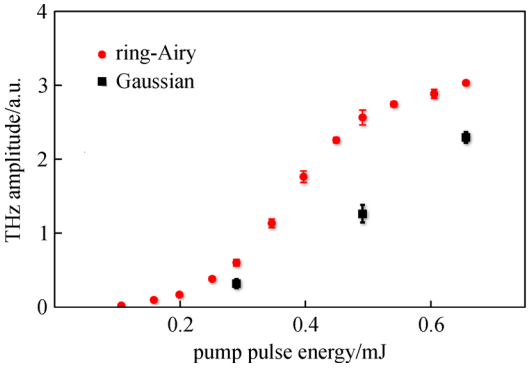

Fig. 13 Comparison between THz emission peak amplitudes from ring-Airy beam and Gaussian beam versus different pump pulse energy

2.5 Numerical simulation

2.5.1 Interference model of terahertz generation from two-color plasmas

To validate our hypothesis on the reasons behind the

enhanced THz radiation pulse energy of ring-Airy beam induced plasma and its red-shifted central frequency, we performed simulations using the interference model, which is able to depict the THz radiation intensity and spectrum of a known plasma [104].

The model is based on the off-axis phase matching theory of two-color laser produced filament [57]. As shown in Fig. 4, the THz radiations emitted from different spots of the filamentation interfere with each other, resulting in a conical radiation pattern in the far field. Since the filament and the generation process should be axially symmetric, the system can be simplified to 2 dimensional, with z as the direction of laser propagation and x the radial axis across it. In this system, the THz wave generated from a spot inside the filament should be proportional to the local nonlinear polarization, which can be expressed as follows:

$$P(x,z,\Omega) \propto A(x,z,\Omega)\sin[\theta(z)]\exp(\mathrm{i}k_{\mathrm{THz}}z), \quad (30)$$

where $A(x,z,\Omega)$ is the generated THz field, Ω is the frequency, and $\sin[\theta(z)]$ is the THz amplitude modulation due to the relative phase θ between ω and 2ω laser pulses. Taking into account the plasma non-uniformity, the phase θ can be calculated as

$$\theta(z) = \theta_0 + \int_{z_{\max}}^{z} [n_{2\omega}(z') - n_{\omega}]k_{\omega}\mathrm{d}z', \quad (31)$$

where $z_{\max}$ is the location with maximum plasma density. $n_{\omega}(z')$ and $n_{2\omega}(z')$ are respectively the refractive indices for ω and 2ω, each of which can be represented by the sum of contribution from the air $n_{\mathrm{air},\omega,2\omega}$ and the plasma

$$n_{\mathrm{plasma},\omega}(z') \approx \sqrt{1-\frac{\omega_p^2(z')}{\omega^2}}, \quad (32)$$

where $\omega_p(z')$ can be calculated with the well-known relation

$$\omega_p = \sqrt{4\pi e^2 N_e(Z')/m_e}. \quad (33)$$

To calculate far-field THz distribution, the THz radiation from each point of the plasma is integrated over the whole filament:

$$E(r,\Theta,\Omega) \propto k_{\mathrm{THz}}\int_V \frac{P(r',\Omega)\exp(\mathrm{i}k_{\mathrm{THz}}|r-r'|)h(r',r,\Omega)}{|r-r'|}\mathrm{d}^2r', \quad (34)$$

where r is the point of detection, r' is the point of emission inside the filament, and h is a factor describing whether the generated THz wave gains an additional phase as it transmits through the plasma or gets screened by the plasma due to afrequency lower than the plasma frequency. It can be expressed as follows:

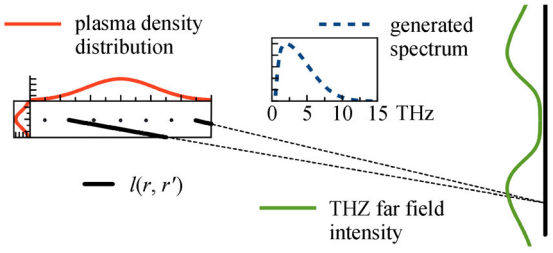

Fig. 14 Schematic representation of two-color filament THz generation interference model (Reprinted from Ref. [104])

$$h(r',r,\Omega) = \begin{cases} 0, & \Omega < \omega_p, \\ \exp\left[\mathrm{i}\int_{l(r,r')} k_{\mathrm{THz}}[n_{\mathrm{THz}}(\xi,\Omega)-1]\mathrm{d}\xi\right], & \Omega \geqslant \omega_p, \end{cases} \quad (35)$$

where l is the ray path between r and r' (see Fig. 14), and n_{THz} is the refractive index the THz wave sees inside the plasma:

$$n_{\mathrm{THz}}(\xi,\omega) = \frac{1}{\sqrt{1-\dfrac{\omega_p^2(\xi)}{\Omega^2}}}. \quad (36)$$

Then the far-field THz radiation intensity can be expressed as a sum of all different frequencies:

$$I(r,\Theta) = \sum\nolimits_{\Omega}|E(r,\Theta,\Omega)|^2 a(\Omega). \quad (37)$$

2.5.2 Simulation results

Using the plasma distributions according to the fluorescence images and the numerical estimations of the maximum electron densities for the Gaussian beam (10^{17} cm^{-3}) and the ring-Airy beam (3×10^{16} cm^{-3}), taking into account the detection band width limitation of a 3-mm-thick ZnTe crystal, the resulting simulated THz radiation pulse energy of a ring-Airy beam induced plasma is found to be about 4 times larger than that from the Gaussian plasma source. The normalized calculations of THz radiation spectra from these two THz sources are shown in Fig. 15(b), giving the same type of central frequency difference as experimental measurements display. Both simulation results agree qualitatively well with the measured data. In addition, to predict the THz sources' behavior when using broadband detection method such as THz-air-biased-coherent-detection [53] or interferometric detection [38], we also performed a full spectral simulations without ZnTe's bandwidth limit, which indicates that the intensity enhancement and the red-shift of the ring-Airy beam induced THz radiation would persist regardless of the detection method. Figure 15(a) showing the normalized

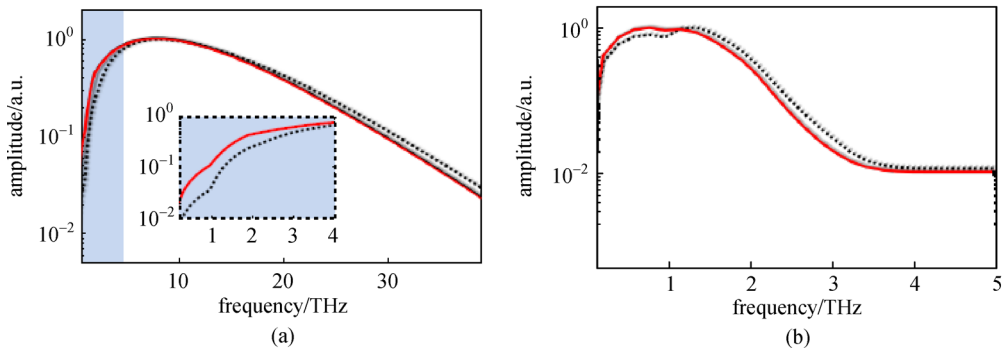

Fig. 15 (a) Normalized simulations of THz radiation spectrums without and (b) with the 3-mm-thick ZnTe detection bandwidth limitation; the inset in (a) is the enlarged version of the blue area (0–4 THz). Red solid curves: emission from ring-Airy plasma; black dashed curves: emission from Gaussian plasma

full spectrum results with an inset focusing on the low frequency region helps to reveal that the ring-Airy beam induced THz radiation spectrum would still have a red-shift comparing to the Gaussian one. This spectral shift to the low frequency could possibly benefit the THz radiation enhancement of ring-Airy beam induced plasma that we measured in the low frequency region. Even so, considering 0.1–3 THz is the most commonly used and more advantageous frequency range for THz time-domain spectroscopy [1], the enhancement we achieved through using ring-Airy beam is still exciting.

2.6 Section summary

In conclusion, ring-Airy beams were utilized to generate enhanced THz radiation from their laser-induced air-plasma, in comparison to normal Gaussian beams. We observed that under the same experimental conditions with 0.5 mJ input pulse energy, the ring-Airy plasma generated THz pulse energy is about 5.3 times larger than that from the Gaussian beam, possibly due to the significant plasma length difference. There is a noticeable change in the THz radiation spectrum between the ring-Airy beam and the Gaussian beam that could be attributed to the plasma density difference between the corresponding plasmas. This unique wavepacket based THz emitter demonstrates the possibility of ring-Airy beam application in the THz frequency remote sensing that will enable high level of control on the excitation beam. It sets a reference for future works involving using different novel wavepackets to tailor the plasma as a THz source. Systematic exploration of the optimum ring-Airy beam parameters for THz generation will possibly entail a further enhancement of the THz radiation. Other families of beams may also exhibit interesting physics in regard to THz generation, such as 2D Airy beams [94] or Airy-Airy-Airy light bullets [83]. As more types of novel beams have been reported, using tools like Spatial Light Modulators or phase masks to sculpt the excitation beams could be a new direction for controlling THz radiation from laser-induced plasma.

3 Terahertz-radiation-enhanced-emission-of-fluorescence of air-plasma in co-propagation geometry

When intense femto-second laser pulses are focused into the air, a laser-induced air plasma is visually observable due to its fluorescence emission. The fluorescence spectral lines between 300 and 500 nm are assigned to the first negative band system of $N_2^+(B^2\sum_u^+ - X^2\sum_g^+$ transition) and the second positive band system of $N_2(C^3\Pi_u - B^3\Pi_g$ transition) [105]. As shown in Fig. 16, the two band systems are respectively marked as "1" and "2". In the parenthesis, v-v′ denotes the vibrational levels of upper and lower electronic states, respectively.

The excitation process of the N_2 molecular ion to the vibrational levels of the $B^2\sum_u^+$ electronic state of N_2^+ that emits in the first negative band system, is mainly achieved through multi-photon ionization of the inner valence electrons from the N_2 molecules. On the other hand, the mechanism of populating the vibrational levels of the $C^3\Pi_u$ electronic state of N_2 that radiates in the second positive band system, is not yet clearly defined. There are evidences suggesting that the mechanism might be some highly excited electronic singlet states got transferred to the triplet electronic state $C^3\Pi_u$ through collision-assisted intersystem crossing.

The interaction between the THz pulse and laser-induced air-plasma has been studied through those fluorescence lines of N_2 between 320 to 400 nm, including 337, 353, 357, 375, 380 and 391 nm (Fig. 17(b)) [60]. During the THz cycle, the electrons trapped in high-lying Rydberg states of the atoms and molecules existing in the plasma can be easily "kicked" into ionic states via collisions with energetic electrons that are heated by the THz radiation. The collision-assisted ionization of these high lying states will lead to the increase of the ion population and therefore results in an enhanced fluorescence radiation, namely THz-radiation-enhanced-emis-

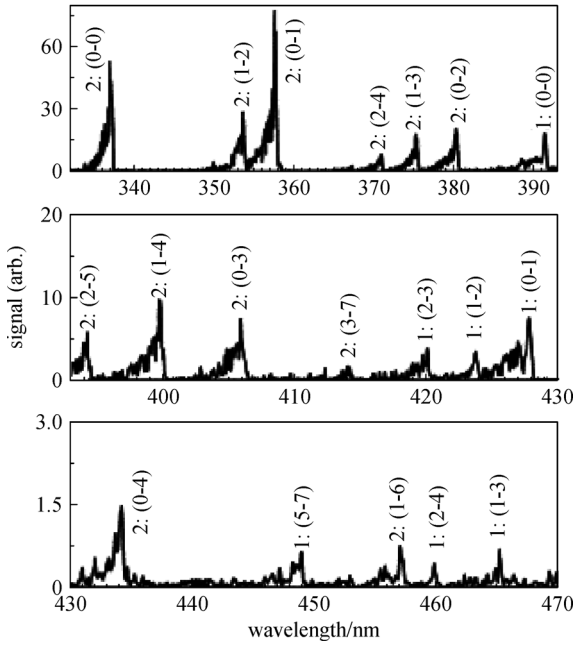

Fig. 16 Spectrum of air interacting with a 220 fs laser pulse. The lines marked by 1 are assigned to the first negative band system of $N_2^+(B^3\sum_u^+ - X^2\sum_g^+$ transition) and those marked by 2 are assigned to the second positive band systemof $N_2(C^3\Pi_u - B^3\Pi_g$ transition) respectively. In the transitions (v–v′), v and v′ denote the vibrational levels of upper and lower electronic states, respectively (Reprinted from Ref. [105])

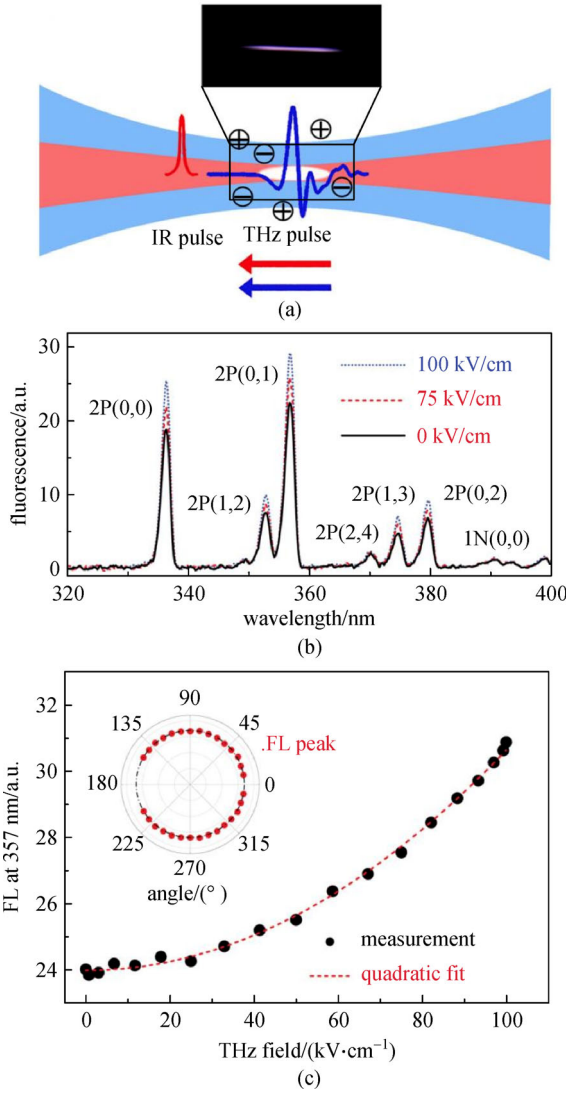

Fig. 17 (a) Schematics of the interaction between the THz wave and laser induced plasma. (b) Measured fluorescence spectra versus THz field as $t_d = -1$ ps. Major fluorescence lines are labeled. (c) Measured quadratic THz field dependence of 357 nm fluorescence emission line as $t_d = -1$ ps. Inset: Theisotropic emission pattern of THz-REEF (Reprinted from Ref. [60])

sion-of-fluorescence (THz-REEF). The fluorescence enhancement is omnidirectional (Fig. 17(c)), and can be used to retrieve the waveform of THz field. To explore the possibility of coherent detection of THz waveform, both one-color and two-color laser excitations were used to generate air-plasma [61].

3.1 One-color scheme

In the case of one-color laser induced plasma, the influence of the THz pulse on the plasma was experimentally investigated, with the experimental setup shown in Fig. 17 (a). The peak THz electric field amplitude reached 100 kV/cm by focusing the pulse into the plasma region. The plasma is generated by focusing a 100 J 100 femto-second laser pulse at 800 nm. Only the situation where the laser pulses propagate collinearly with the THz pulse, namely co-propagation geometry, is discussed. The plasma fluorescence spectrum was measured by a monochromator with a photo multiplier tube (PMT) attached. The THz time-domain waveform was also measured by electro-optic (EO) sampling as reference [39].

The experimental setup works as a pump-probe system with the temporal delay between THz pulse and the laser pulse, t_d, well controlled by a delay stage. The t_d is defined such that when it is negative, the THz pulse arrives later than the laser pulse at the plasma region; when it is positive, the THz pulse arrives earlier than the laser pulse at the plasma region.

Figure 17(b) shows that the fluorescence lines between 320 and 400 nm are enhanced by the THz pulse and the enhancement would increase as the THz field goes higher. As further explained in Fig. 17(c), the fluorescence intensity at 357 nm increases quadratically as the THz pulse peak amplitude increases.

Figure 18 shows the measured time-resolved fluorescence enhancement $\Delta FL(t_d)$ signal plotted against the time-resolved THz field waveform $E_{THz}(t_d)$ measuredby EO sampling. When the THz pulse is ahead of laser pulse, $\Delta FL(t_d) = 0$, sincethe THz pulse does not see the plasma when it passes the plasma region, therefore gives no

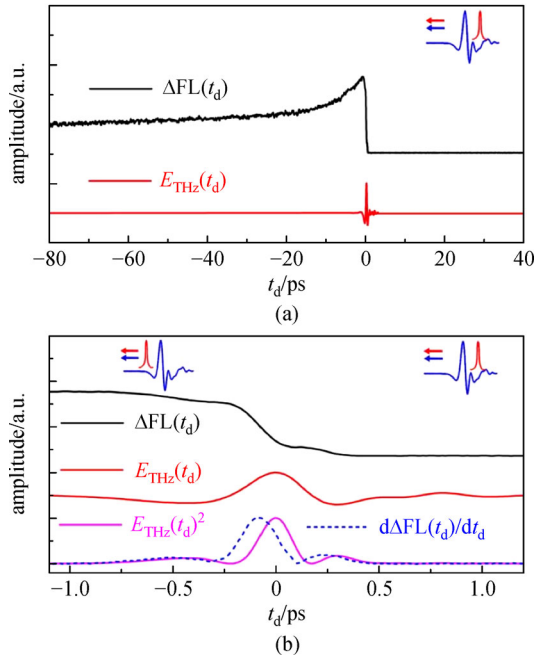

Fig. 18 (a) Time-resolved THz-REEF $\Delta FL(t_d)$ and THz field $E_{THz}(t_d)$. (b) Time-resolved $\Delta FL(t_d)$, $E_{THz}(t_d)$, $d\Delta FL(t_d)/dt_d$, and $E^2_{THz}(t_d)$ on therising edge in the expanded scale of (a). All curves are normalized and offset forclarity (Reprinted from Ref. [60])

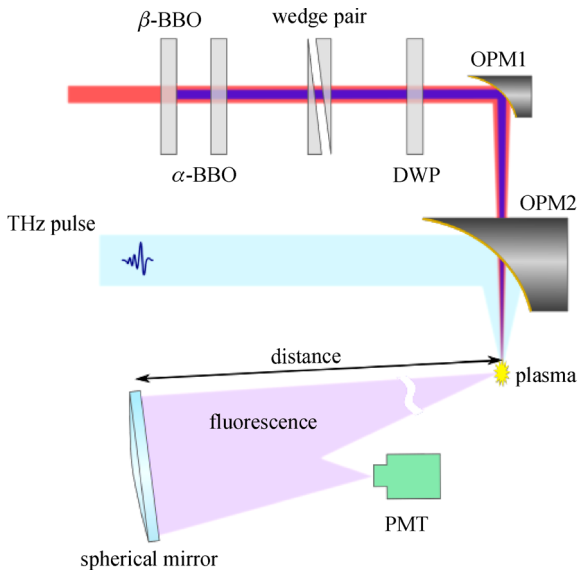

Fig. 19 Schematic figure of THz-REEF remote sensing experimental setup. DWP: dual wave plate; OPM: off-axis parabolic mirror; PMT: photo multiplier tube detector

enhancement of the fluorescence. However, $\Delta FL(t_d)$ shows a rapid increase as the THz pulse and the laser pulse start to temporally overlap and reaches the maximum as the laser pulse coincides with the beginning of the THz pulse, see Fig. 18(b). As the time delay t_d goes to the negative regime, $\Delta FL(t_d)$ slowly decreases as $|t_d|$ increases, since the plasma is going through relaxation after the excitation laser pulse passes by the focus area. Also shown in Fig. 18(b) in the bottom, the time derivative of the enhanced fluorescence is found to be proportional to the square of the THz waveform. To explain the above observation, the $\Delta FL(t_d)$ can be expressed as

$$\lim_{\tau \ll \tau_{THz}} \Delta FL \propto n_e(\beta_{ei}, t_d)\frac{e^2\tau}{2m}\int_{t_d+t_\varphi} E^2_{THz}(t)dt, \qquad (38)$$

where n_e is the electron density, β_{ei} is the electron-ion recombination rate, e is theelectron charge, m is the electron mass, τ is the electron collision relaxation time, and t_φ is the phase delay caused by the plasma formation dynamics at the earlystage. It shows that the ΔFL is proportional to the integration of square of theTHz field.

3.2 Two-color scheme

In last section, the one-color THz-REEF technique was introduced. However, this method only detects THz intensity without the phase information, which makes it not ideal for coherent remote sensing due to its need of an external local oscillator. On the other hand, the two-color THz-REEF exploits a symmetry-broken laser excitation to drive the electrons and naturally detects THz field coherently.

In the two-color scheme of THz-REEF technique, β-BBO is used to generate second harmonics 2ω from the fundamental ω beam. As shown in Fig. 19, a set of phase controlling system, including an α-BBO, a pair of silica wedges anda dual wave plate (DWP), is also used to control the walk-off effect and fine-tune the relative phase between ω and 2ω. The rest of the set-up is similar with the one-color THz-REEF.

Same with the one-color THz-REEF, in the two-color scheme, the THz pulse heats up the ionized electrons, resulting in further ionization of the electrons trapped in the high-lying excited states through electron impact. However, with two-color laser excitation, the ionized electrons will acquire an asymmetric drift velocity, whereas with one-color multi-cycle laser pulse, the ionized electrons will be given a symmetric drift velocity. The drift velocity distribution can be controlled by the relative phase of two color pulses, $\varphi_{\omega,2\omega}$. With asymmetric electronvelocity, parallel or anti-parallel THz field polarity will result in acceleration or deceleration of the electrons, as shown in Fig. 20(b), therefore affecting the enhancement of the fluorescence. In this way, the THz field information can be successfully encoded into the fluorescence enhancement signal. Figure 21 is showing how different $\varphi_{\omega,2\omega}$ is affecting the time-dependent REEF curve. The modulated purple dots could be the intensity of THz generation from the two-color plasma or its fluorescence emission, either of which can be used as an indicator of the two-color pulse relative phase during the experiment.

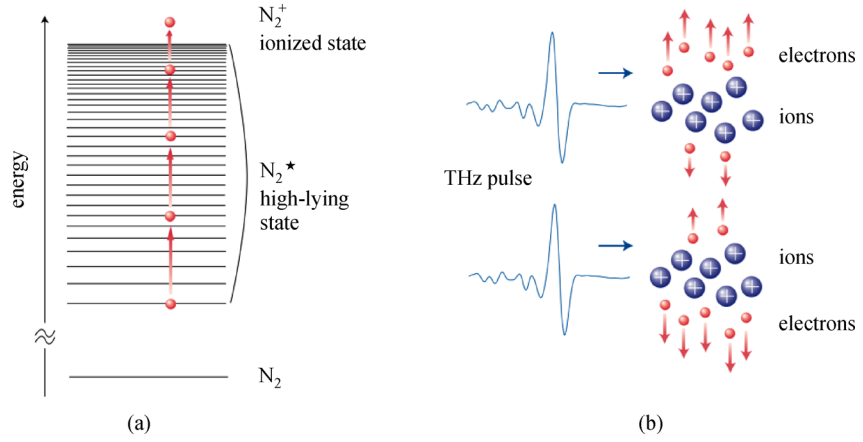

Fig. 20 Terahertz wave assisted electron impact ionization of high-lying states in plasma. (a) High-lying states can be ionized by a series of collisions with energetic electrons; (b) interaction between the terahertz pulse and the asymmetric photoelectron velocity distributions generated by two-color field ionization (Reprinted from Ref. [61])

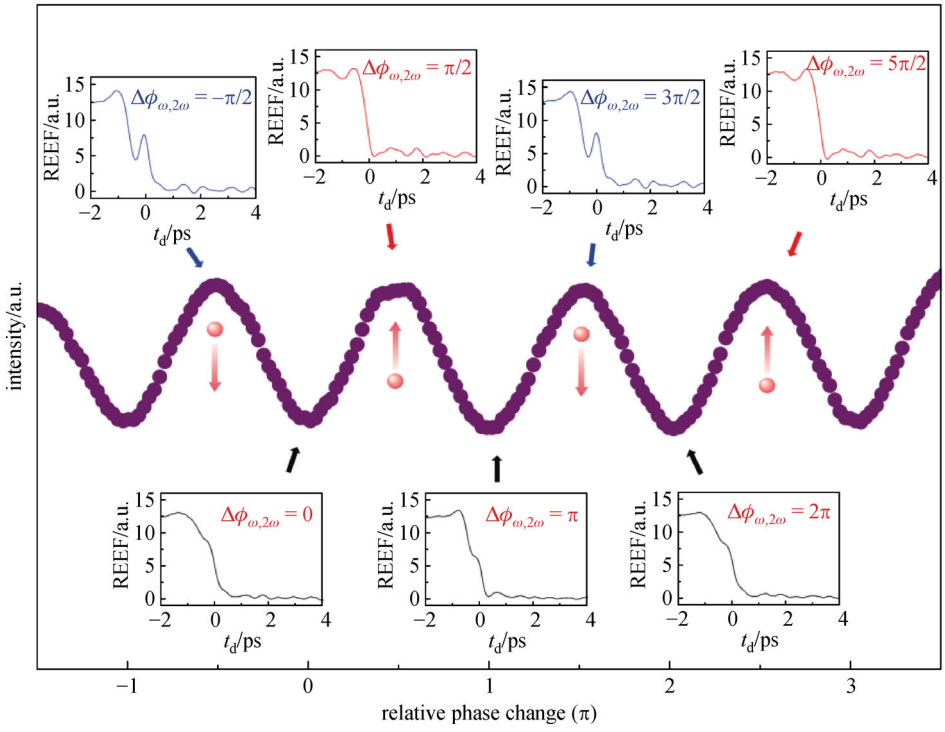

Fig. 21 Measured time-dependent REEF at a relative optical phase change of $\Delta\varphi_{\omega,2\omega} = \pm m\pi/2$. The terahertz wave enhanced fluorescence shows significantdependence on the initial electron velocity distribution, which is determined by $\Delta\varphi_{\omega,2\omega}$ (Reprinted from Ref. [61])

The THz pulse waveform information can be directly retrieved by taking the difference between $\Delta I_{\mathrm{FL}}(\Delta\varphi_{\omega,2\omega} = \pi/2)$ and $\Delta I_{\mathrm{FL}}(\Delta\varphi_{\omega,2\omega} = -\pi/2)$, as shown in Fig. 22.

To describe the above observation, the photo-emission enhancement can be expressed as proportional to the total kinetic energy transferred to the electrons in a long period of time:

$$\Delta I_{\mathrm{FL}}(\Delta\varphi_{\omega,2\omega}) \propto n_{\mathrm{e}}\left[\int_{-\infty}^{+\infty}\left(m_{\mathrm{e}}\vec{v}^{2}(0) + 2m_{\mathrm{e}}\vec{v}(0)\Delta\vec{v}_1\right)\rho\left(\vec{v}(0),\Delta\varphi_{\omega,2\omega}\right)\mathrm{d}\frac{\vec{v}(0)}{2} + m_{\mathrm{e}}\sum_{i=1}^{\infty}\Delta\vec{v}_i^{2}\right]. \tag{39}$$

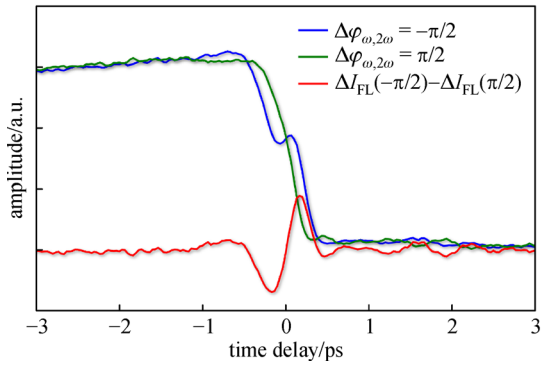

Fig. 22 Typical two-color THz-REEF signal. Blue and green: two THz-REEF traces with different relative phase $\Delta\varphi_{\omega,2\omega}$. Red: the difference between blue andgreen curves, that gives the measured THz waveform

where n_e is the electron density and $\Delta\vec{v}_i = -\int_{t_i-\tau}^{t_i}\vec{E}_{THz}(t)dt/m_e$ which is the electron velocity gained by acceleration from the THz field. The $m_e\vec{v}^2(0)$ term is the initial electron kinetic energy gained from the laser excitation, ρ is the electron velocity distribution depending on $\varphi_{\omega,2\omega}$. Applying the symmetry $\rho\left(\vec{v}(0),\pi/2\right) = \rho\left(\vec{v}(0),-\pi/2\right)$ to the above equation we get

$$\Delta I_{FL}\left(\Delta\varphi_{\omega,2\omega} = -\frac{\pi}{2}\right) - \Delta I_{FL}\left(\Delta\varphi_{\omega,2\omega} = \frac{\pi}{2}\right) \propto n_e\rho\tau\vec{v}_e\vec{E}_{THz} \propto \vec{E}_{THz}. \quad (40)$$

3.3 Terahertz remote detection at 30 m

As mentioned in Section 1, the bottleneck of stand-off remote sensing of THz radiation is how to pass the THz wave form information remotely without undergoing with the atmosphere attenuation by water vapor absorption. In THz-REEF technique, the use of UV fluorescence emitted by the plasma as the carrier of spectroscopic THz wave form information can help us circumvent this obstacle, due to the fact that UV light has very low absorption rate in water vapor.

In the past work by Liu et al. [61], a remote detection of THz waveform at 10 m was demonstrated as a proof of principle for THz stand-off detection by two-color THz-REEF technique. The distance of THz remote detection by THz-REEF has been pushed to 30 m, with a better arrangement and alignment of the collection optics. Notice that the detection distance is defined as the distance between the plasma, which is the UV source, and the final collecting mirror with focusing power, as notified in Fig. 19.

The work was conducted in a two-room laboratory space with the excitation laser pulse source (800 nm 100 fs Ti: Sapphire laser) and the THz pulse source ($LiNbO_3$ crystal with pulse front tilting set-up) located in one room, as well as multiple Aluminum coated flat mirrors located in both rooms folding the beam path in order to create 30 m distance. The collecting efficiency was eventually limited by a parabolic mirror (replacing the spherical mirror in Fig. 19) with 15 inch diameter and 60 inch focal length. The collected UV light was focused into a PMT detector to measure the THz-REEF signal. During the alignment of the mirrors, a high intensity LED light source with an iris diaphragm was used to mimic the plasma source in order to create better visibility of the beam path. With the assistance of the LED source, a reference focal point of the beam was marked up before further fine adjustments of the PMT position, height and angle were made in order to catch the weak THz-REEF signal, due to the fact that only a small solid angle (0.000126) of the radiation has been collected.

In Fig. 23, the THz wave forms measured by two-color THz-REEF technique at different distances from 0.1 to 30 m are shown together. For the 30 m data, a dynamic range of 4, which is the ratio between the signal peak and the signal variation of the baseline, was achieved. This indicates all air-plasma stand-off THz wave remote sensing at 30 m is feasible in the laboratory. Considering the reflection loss of the multiple folding mirrors and the limitation of the final collecting parabolic mirror, this distance has the potential to be further increased either in the laboratory or in the field. With certain engineering techniques, such as shaking the silica wedge of the two-color beam phase controller at certain modulation frequency in order to reduce the scan number to retrieve one THz wave form from dual-scan to single-scan [106], the signal scanning speed can be largely improved, therefore the dynamic range of a signal acquired within a certain amount of time could be improved.

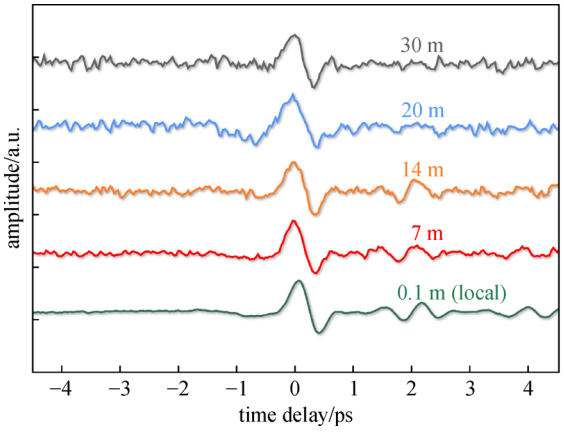

Fig. 23 THz waveforms measured by two-color THz-REEF technique at different detection distances, 0.1, 7, 14, 20, 30 m respectively

4 Terahertz-radiation-enhanced-emission-of-fluorescence of air-plasma in counter-propagation geometry

In 2010, the coherent remote sensing of broadband THz wave using the special technique of THz-radiation-enhanced-emission-of-fluorescence (THz-REEF) was reported. However, its application in homeland security or environmental monitoring is hindered by the fact that so far the THz-REEF detection was only performed in a co-propagation geometry, where the THz pulses travel collinearly with the probe pulses. In reality, when THz pulses are reflected by the target, they travel in the opposite direction with the probe pulses, resulting a counter-propagation situation.

The study of THz-REEF in co-propagation geometry, including one-color and two-color schemes and 30 m remote sensing, is introduced in last section. In this section, the interaction between THz pulse and laser induced air plasma fluorescence emission in the counter-propagation manner will be experimentally demonstrated with comparison between the co-propagation and the counter-propagation geometries [107]. Furthermore, systematic exploration of its mechanism and applications is also performed.

4.1 Terahertz-REEF of elongated plasmas in counter-propagation geometry

First of all, we have compared the counter-propagation THz-REEF signal with the conventional co-propagation THz-REEF signal of an elongated plasma. Following a method similar to that of co-propagation THz-REEF, the setup implements the standard pump-probe THz time-domain spectroscopy technique. The laser source (100 fs 800 nm Ti-Sapphire laser) is bifurcated by a beam splitter into pump and probe beam. The pump beam is sent to a piece of $LiNbO_3$ crystal to generate strong THz pulse with >100 kV/cm peak electric field using pulse-tilting technique. The probe beam is focused by a 4-inch (101.6 mm) focal length lens in order to generate plasma in the ambient air. A translational stage controls the time delay Δt between the pump and probe beam. In the co-propagation setup, the THz pulse was focused collinearly with the probe beam onto the plasma by a gold 2-inch (50.8 mm) focal length off-axis-parabolic-mirror. The parabolic mirror has a small hole in the middle to let the probe beam pass but not lose too much THz pulse energy. However, when making the counter-propagation measurement, the THz pulses are focused by the parabolic mirror from the opposite direction such that the spatial overlap between the THz focal volume and the probe beam focal volume is maximized. In both cases, the fluorescence emission from the plasma is sent through a monochromator and measured by a photomultiplier tube (PMT). Both of the cases are depicted in Figs. 24(b) and 24(d).

The comparison between the time-resolved THz REEF data $\Delta I_{FL}(\Delta t)$ in the two cases are presented in Figs. 24(a) and 24(c). The REEF traces are obtained by measuring the intensity of the fluorescence emission line centered at 337 nm which belongs to the second positive band system of N_2, as a function of the timedelay, Δt, between the THz and the optical pulses. Both traces exhibit significant THz-induced enhancement of the fluorescence intensity as the THz is interacting with the plasma. Other than the similar enhancement effect, it can be observed obviously that in the two different cases the enhancement arising curves where the THz pulses arrive around similar time as the probe beam thus interact with it actively, show different slopes. For the co-propagation THz-REEF signal (see Fig. 24(a)), the arising curve from minimum to maximum takes about 2 ps. For the counter-propagation signal (see Fig. 24(c)), it takes as long as 10 ps. In the co-propagation case, the delay time Δt is defined such that for positive value, the THz pulse arrives at the focal spot ahead of the probe beam, therefore there is no enhancement effect. When it is negative, the THz pulse arrives later than the probe beam that generates the plasma, and there will be fluorescence enhancement due to the THz-plasma interaction. $\Delta t = 0$ is set to be when optical pulse peak coincides with the THz pulse peak. For a single cycle THz pulse, the time-resolved waveform is normally bipolar. In Fig. 24(a), the $\Delta t = 0$ is set to be when the optical pulse peak coincides with the first pole of the THz pulse. For the counter-propagation case, the Δt is defined similarly, but the zero point is arbitrarily defined when the two pulses meet at the midpoint of the plasma.

This discrepancy on the enhancement arising slopes originates from the different probing effect provided by the two THz-REEF configurations. In the co-propagation one, Δt is the time delay between the peaks of the two pulses as theytravel in the same direction. Positive values are defined such that the THz pulse leads the optical pulse. When $\Delta t = t_1$ where the enhancement ΔI_{FL} starts to riseabove the baseline in Fig. 24(a), it is corresponding to the case when the optical pulse starts to catch the tail of the THz pulse, as shown in Fig. 24(b) top scheme. When $\Delta t = t_2$ where the enhancement ΔI_{FL} reaches the maximum, it is corresponding to when the optical pulse is completely ahead of the THz pulse, as shown in Fig. 24(b) bottom scheme. Therefore, considering that the optical pulse is much shorter than the THz pulse, in this geometry, the optical pulse is sensing the THz pulse, and the rising curve time duration is equivalent to the THz pulse duration. In the counter-propagating case, for different values of Δt, the THz pulse and the optical pulse meet at different locations of the plasma. When $\Delta t = t_1'$ where the enhancement ΔI_{FL} starts to rise above the baseline in Fig. 24(c), it is corresponding to the case where the optical and the THz pulse meet at the border of the elongated plasma volume such that the optical pulse is entering the volume when the

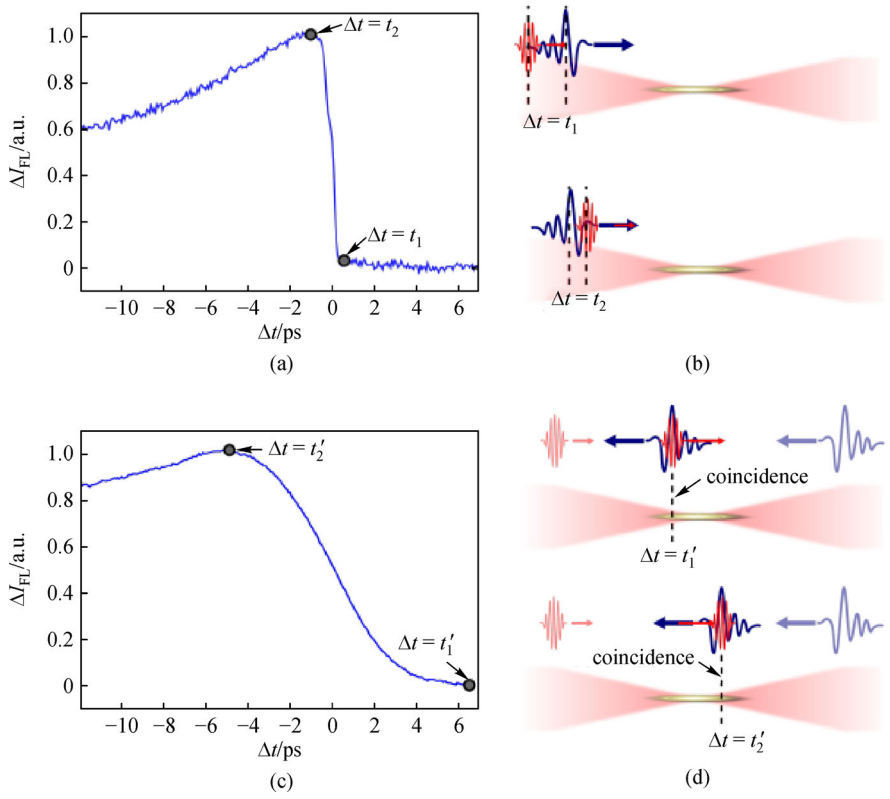

Fig. 24 Depiction of the co-propagation and counter-propagation interaction geometries. (a) and (c) are showing the plasma fluorescence intensity enhancement as a function of Δt in (a) co-propagating and (c) counter-propagating geometriesmeasured by PMT. Both curves are normalized to 1. (b) In co-propagating geometry the THz (blue) and the NIR (red) pulses travel in the same direction. (d) In counter-propagating geometry the THz and NIR pulses travel in opposite directions. Δt is the time delay between the two pulses. The special cases of $\Delta t = t_1$, t_2 in co-propagation or $\Delta t = t_1'$, t_2' in counter-propagation are respectively denoted in (a,b) and (c,d)

THz pulse is leaving it, as shown in Fig. 24(d) top scheme. In this case, the THz pulse does interact with the plasma at all, resulting to no fluorescence enhancement. When $\Delta t = t'_2$ where the enhancement ΔI_{FL} reachesthe maximum in Fig. 24(c), it is corresponding to the case when the optical and the THz pulse meet at the other border of the elongated plasma volume such that the optical pulse is leaving the volume when the THz pulse is entering it, as shown in Fig. 24(d) bottom scheme. In this case, the THz pulse is able to interact with the plasma immediately after it is generated, resulting in the maximum fluorescence enhancement. In this geometry, the THz pulse is actually sensing the plasma. In the counter-propagating geometry the rising time of the REEF trace depends on the length of the plasma, the longer the plasma the longer the rising time, resulting in a trace shape much different compared with the co-propagating one.

Moreover, the slope of the co-propagating trace shows a distinctive feature, which is originated from the typical bipolar waveform of a single cycle THz pulse. The derivative of the curve yields the time-dependent THz pulse intensity as previously demonstrated by Liu and Zhang [60]. However, for the case of elongated plasma generated by 4-inch effective focal length (EFL) lens, the counter-propagating trace is smooth and featureless.

4.2 Terahertz-REEF of micro-plasmas in counter-propagation geometry

To further understand the sensing mechanism of counter-propagation THz-REEF, the length of the plasma is gradually reduced to micro-plasma regime by using different focal length lens. The time-resolved REEF traces measured by PMT of the plasmas obtained with three different focusing elements, 4 inch, 2 inch and 1 inch EFL lenses, are plotted in Fig. 25(d), with Figs. 25(a)−25(c) describing schematically the three plasma generation scenarios. As expected, when the plasma length decreases, the rising time of the fluorescence enhancement curve gets shorter. However, differently from the case of elongated plasmas created by the 4-inch EFL lens, the curves obtained with the micro-plasmas generated by 2 inch and 1 inch EFL lenses display a distinctive undulation on the slope. While it is tempting to attribute this feature to the

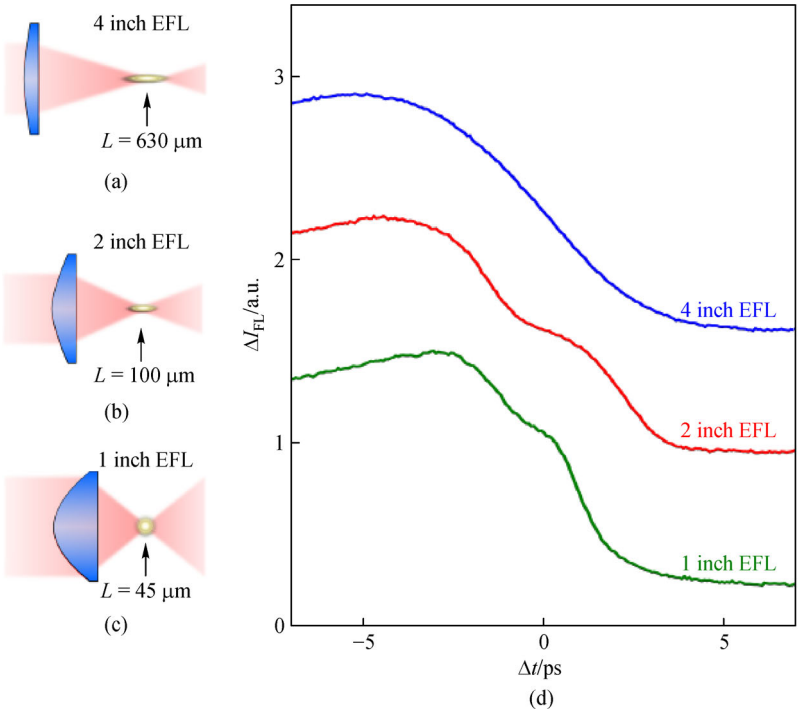

Fig. 25 Schematic demonstrations of plasmas of different lengths being generated by (a) 4 inch EFL, (b) 2 inch EFL, and (c) 1 inch EFL plano-convex lenses. (d) Time-resolved counter-propagation THz-REEF measurements of the plasmas generated in (a)–(c) cases

time-evolution of THz waveform, this conclusion is not supported by the much slower time scale at which this undulation evolves, as shown in Fig. 26.

In Fig. 27, time-resolved counter-propagation THz-REEF signals ΔI_{FL} of 2 inch EFL lens generated micro-plasma are plotted as a function of THz pulsepeak field strength. The result shows that the undulation is not sensitive to the THz field strength change, further proves our hypothesis that this feature is not due to the time-evolution of THz waveform.

Figure 28 shows the micro-plasma fluorescence emission spectra given different plasma excitation pulse energies, with and without the existence of THz pulse. We can observe that for the case of micro-plasma, due to the high local intensity at the plasma volume, the fluorescence spectrum changes when the pulse energy increases. The onset and growth of broadband continuum between 300 and 400 nm eventually deprive the peak enhancement at 337 nm, implying that different ionization mechanisms start to dominate [108].

4.3 Two-color terahertz-REEF in counter-propagation

To explore the possibility of coherent THz detection in

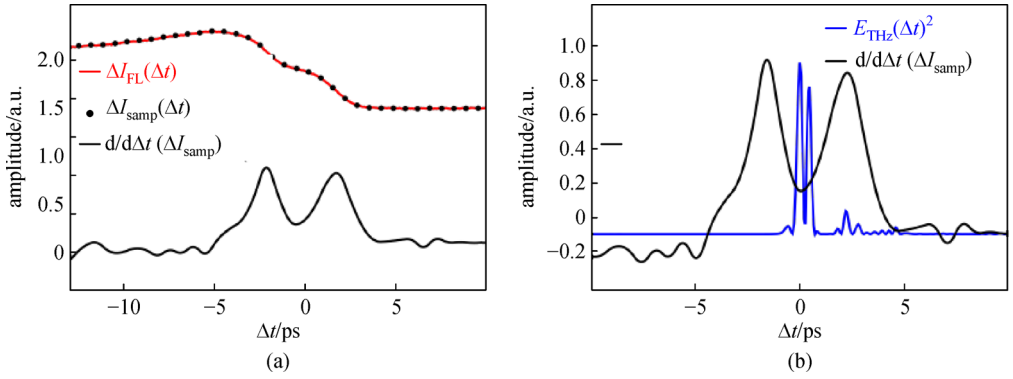

Fig. 26 (a) Time-resolved counter-propagation THz-REEF intensity for 2 inch EFL lens case (solid red) and its derivative (solid black). The black dots represent the data sampling rate used for the derivative in order to reduce the noise of the result. The curves are offset for clarity. (b) Derivative of REEF signal curve (solid black) is compared to the square of the experimental THz waveform measured with electro-optic sampling (solid blue)

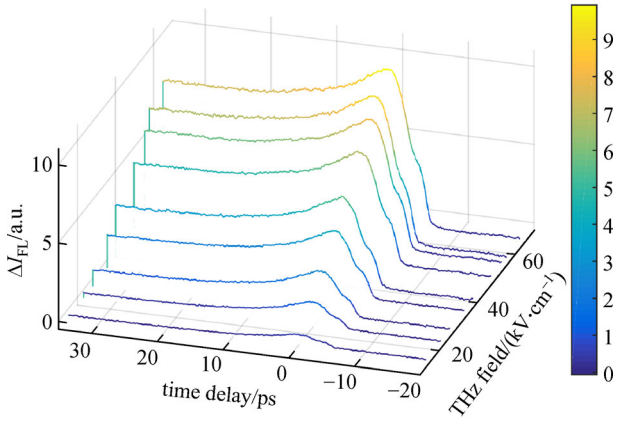

Fig. 27 Time-resolved counter-propagation THz-REEF measurements of a micro-plasma with different THz pulse peak field strengths. The plasma is generated by a 2 inch EFL lens

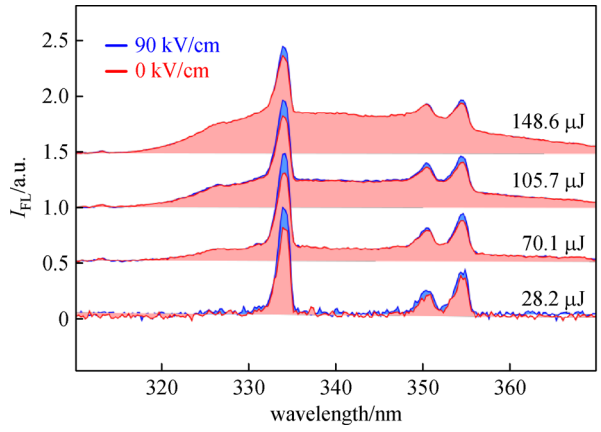

Fig. 28 Micro-plasma fluorescence emission spectra with different values of plasma excitation laser pulse energy. Red is when no THz pulse is applied and blue is when a THz pulse with peak field of 90 kV/cm is applied. The microplasmas are obtained with a 1 inch EFL plano-convex lens

counter-propagation geometry, two-color scheme is also performed with both elongated plasma and microplasma. The experimental setup is similar to that of Fig. 19, except that the THz wave is focused onto the plasma from the opposite direction. A pair of wedges is used to control the phase between ω and 2ω optical pulses. Figures 29(a) and 29(b) are showing the time-resolved counter-propagation two-color THz-REEF measurements of 4 inch EFL lens generated plasma and 2 inch EFL lens generated plasma, respectively. For each set of measurements, different color of traces represents different relative phase $\Delta\phi$ between ω and 2ω. The value of $\Delta\phi$ is determined according to the plasma fluorescence intensity modulation as a function of $\Delta\phi$, as shown in Fig. 29(c). The results show that in counter-propagation case, the THz-REEF trace does not display a dependence on $\Delta\phi$, unlike in the co-propagation case. This is possibly because in counter-propagation

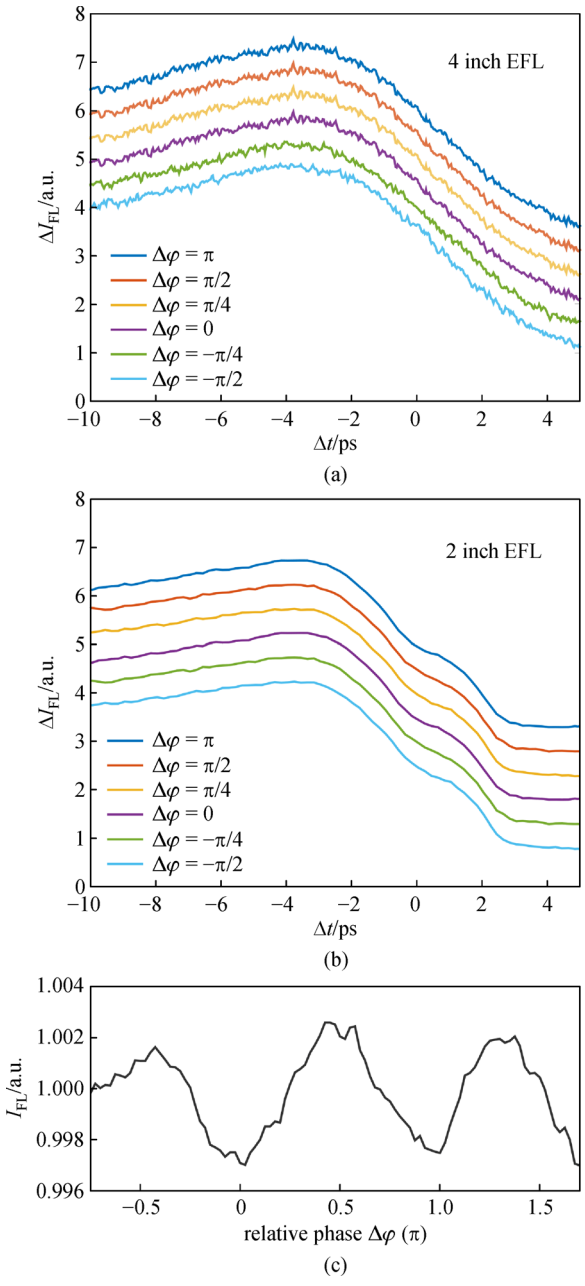

Fig. 29 Time-resolved counter-propagation two color THz-REEF measurements with different phases $\Delta\phi$ between ω and 2ω pulses. The plasma is generated with (a) 4 inch EFL lens and (b) 2 inch EFL lens. (c) Plasma fluorescence intensity modulation as a function of the relative phase $\Delta\phi$

geometry, the THz pulse and the optical pulse do not have a constant phase relation as they propagate. When the THz pulse enhances fluorescence emission as it travels along the plasma, the phase information of the excited electron density has been washed out in the integrated signal. However, in the co-propagation case, the THz pulse and the optical pulses travel with a quasi-constant phase relation. So when the THz pulse travels through the plasma, at each point, it sees the electron density with a

consistent phase. Therefore, the integrated signal still contains the phase information.

4.4 Terahertz-REEF in counter-propagation for plasma diagnosis

To interpret the origin of the shape of the REEF traces obtained in counter-propagating geometry with the micro-plasmas, we modified the math expression describing the REEF traces in co-propagating geometry in the limit of high pressure gas [60,109,110] to include also the space dependencies. The resulting expression for the plasma fluorescence enhancement ΔI_{FL} is

$$\Delta I_{\mathrm{FL}}(\Delta t) \propto \int\int_{-\infty}^{+\infty} n_{\mathrm{e,eff}}\left(z, t-\Delta t \pm \frac{z}{c}\right) E_{\mathrm{THz}}^{2}\left(z, t-\frac{z}{c}\right) \mathrm{d}t\mathrm{d}z, \tag{41}$$

where $n_{\mathrm{e,eff}}$ is the effective electron density contributing to the fluorescence intensity change through THz-REEF and E_{THz} is the THz pulse electric field. By changing the sign in front of the propagation term $\frac{z}{c}$ inside of $n_{\mathrm{e,eff}}\left(z, t-\Delta t \pm \frac{z}{c}\right)$, the equation can respectively describe the counter-propagation geometry (plus sign) and co-propagation geometry (minus sign). Through a least square fitting algorithm, Eq. (41) is employed to retrieve hypothetical electron density spatial profiles $n_{\mathrm{e,eff}}(z)$ that would result in the measured REEF traces in the cases of the two micro-plasmas. For this purpose we used the time dependence for n_{e} discussed in Ref. [60] and the THz electric field measured with EO sampling. The fitted curves and the respective computed plasma profiles, compared with the fluorescence profiles measured with the iCCD camera are shown in Fig. 30.

Instead of representing the actual electron density spatial distribution, those curves are to be interpreted as the effective electron densities contributing to the REEF signals. As we can see, the computed $n_{\mathrm{e,eff}}$ and the measured fluorescenceprofiles differ dramatically in the cases of micro-plasmas. In particular those curves suggest that the denser part of the plasma has very little contribution to the fluorescence enhancement, whereas the biggest contribution is due to the interaction of the THz wave with the outer region of the plasma, where the electron density is lower. This could be qualitatively explained by two physics phenomena: 1) the volumes with highest electron densities are the ones presenting the highest degree of ionization of the air molecules. It is therefore plausible that the contribution of those volumes to the THz-REEF signal is very small, as the density of electronic states right below the continuum (~100 meV), which are the one contributing to the THz induced fluorescence enhancement [61], is greatly reduced for highly ionized molecules. 2) For values of electron densities higher than 10^{16} cm^{-3}, which are achieved in the experiment being discussed, the plasma frequency becomes greater that 1 THz. Frequencies below that value are not allowed to propagate through the plasma, but they decay exponentially within a space defined by the skin

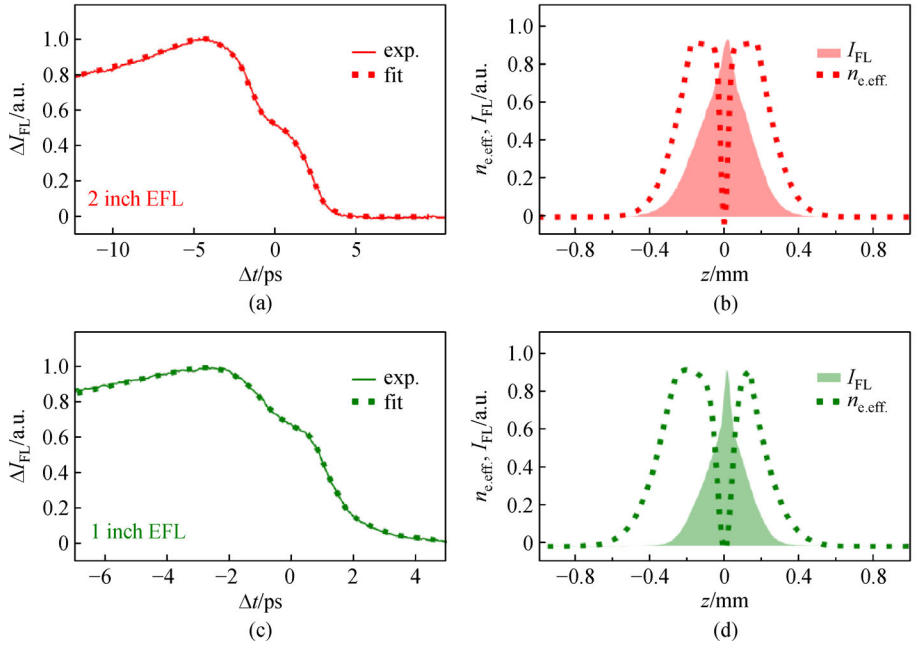

Fig. 30 Experimental (solid line) and numerical fitted (dashed line) time resolved counter-propagation THz-REEF intensity for the following focusing conditions: (a) 2 inch EFL lens; (c) 1 inch EFL lens; in (b), (d), the solid shaded areas represent the integration of the plasma fluorescence intensity along the radial dimension as measured with the iCCD camera, and the dashed lines are the numerically evaluated plasma effective electron densities producing the dashed curves plotted in (a) and (c)

depth of the plasma at the specified frequency. The skin depth gets smaller as the electron density increases. For the estimated electron densities of the experiment and the peak frequency of the input THz pulse (0.7 THz), the skin depth in the densest volume is as low as 5 μm. Therefore the densest part of the plasma is screened from the incoming THz pulse and do not contribute to the THz-REEF signal.

4.5 Section summary

THz-REEF in counter-propagating geometry is demonstrated with both elongated plasmas and micro-plasmas. The THz-REEF traces in counter-propagation geometry for elongated plasma do not explicitly contain any feature related to the time evolution of the measured THz pulse, whereas in the case of micro-plasmas, the THz-REEF trace shows distinctive undulation features in the slope. Those features, together with the rising time of the fluorescence enhancement, can be reproduced by the computation of hypothetical effective electron density distributions, suggesting that the densest volumes of the plasma possibly do not contribute to the THz-REEF signal. Due to the inconclusive nature of findings, further experiments are necessary to confirm this hypothesis with the help of high resolution CCD camera and further manipulation of the plasma. The results presented herein suggest the counter-propagating REEF is a good candidate as a tool for plasma diagnostics, for it essentially allows the THz radiation as a probe to sense the electron density and dimension of the plasma in question. Resolving the THz intensity evolution in the counter-propagating geometry will possibly be allowed for plasmas short enough to timely resolve the THz electric field changes.

5 Conclusions

THz generation and detection techniques for the purpose of THz wave stand-off sensing with air-photonics techniques are reviewed. Intense laser induced air plasma has been engineered into different shapes in order to enhance THz wave generation as well as to detect THz in unconventional but more practical configuration.

For THz generation, laser induced air-plasma is further explored as a source of remote THz emitter. With the use of abruptly auto-focusing ring-Airy beam, a factor of five of the enhancement of THz pulse energy has been realized while are shifted on the THz emission spectrum is also observed. With the interference model, we were able to qualitatively repeat our experimental data in spectral domain. Furthermore, as a potential beam for remote plasma generation that can provide robustness, flexible tunability, and high-contrast focus intensity, ring-Airy beam nonlinear propagation in air was also experimentally demonstrated. Different ring-Airy beam generation methods were also introduced and evaluated for their potentials in ultrafast intense optics. For THz detection, first THz remote sensing through two color THz-REEF technique was demonstrated at 30 m. To further the development in THz remote sensing technique, THz-REEF in counter-propagation geometry, a detection configuration more realistic than the conventional co-propagation geometry, has been studied. Different time-resolved counter-propagation THz-REEF traces generated by plasmas with different lengths were compared with the co-propagation REEF trace, with the finding that the counter-propagation REEF trace shape is an indicator of the plasma's length and intensity distribution, implying potential applications in plasma diagnostics. THz field dependent study and two-color phase modulation study on the counter-propagation REEF traces did not show any explicit sign of coherent modulation by THz field.

As a final conclusion, we can see that the pros of generating terahertz from ring-Airy beams and detecting terahertz by THz-REEF of air-plasma in co-propagation geometry and of air-plasma in counter-propagation geometry are as follows:

1) Under the same experimental conditions with the same input pulse energy, the ring-Airy plasma generated THz pulse energy is up to about five times larger than that from the Gaussian beam.

2) Intensity enhancement and the red-shift of the ring-Airy beam induced THz radiation would persist regardless of the detection method.

3) The spectral shift to the low frequency could possibly benefit the THz radiation enhancement of ring-Airy beam induced plasma that we measured in the low frequency region.

4) The possibility of ring-Airy beam application in the THz frequency remote sensing that will enable high level of control on the excitation beam.

5) In THz- REEF technique, the use of UV fluorescence emitted by the plasma as the carrier of spectroscopic THz wave form information can help us circumvent this obstacle, and the distance of THz remote detection has been pushed with a better arrangement and alignment of the collection optics.

6) The counter-propagating REEF allows the THz radiation as a probe to sense the electron density and dimension of the plasma in question and resolving the THz intensity evolution in the counter-propagating geometry will possibly be allowed for plasmas short enough to timely resolve the THz electric field changes.

The cons of the researched methods may be

1) The ring-Airy plasma THz emission has a central frequency slightly lower than the Gaussian one, which denotes that the ring-Airy plasma has a lower plasma density.

2) At the same focusing condition, the THz generation saturation threshold of the ring-Airy beam induced plasma is lower than the Gaussian plasma, possibly due to the

easier onset of intensity clamping effects in plasmas and nonlinear interaction with lenses by the special intensity structure of ring-Airy beams.

This review may help us deepen understanding of terahertz air photonics and terahertz wave information remote detection and demonstrate the bright future of terahertz science and technology.

Acknowledgements This research was sponsored by the Army Research Office and was accomplished under Grant Nos. US ARMY W911NF-14-1-0343, W911NF-16-1-0436, and W911NF-17-1-0428. And we would like to appreciate the National Natural Science Foundation of China (NSFC) for supporting Pingjie Huang (Grant Nos. 61473255 and 61873234).

References

1. Zhang X C, Xu J. Introduction to THz Wave Photonics. New York: Springer, 2010
2. Zhang X C. Teaching note, 2013
3. Fixsen D J, Cheng E S, Gales J M, Mather J C, Shafer R A, Wright E L. The cosmic microwave background spectrum from the full cobefiras data set. Astrophysical Journal, 1996, 473(2): 576–587
4. Leisawitz D T, Danchi W C, DiPirro M J, Feinberg L D, Gezari D Y, Hagopian M, Langer W D, Mather J C, Moseley S H, Shao M, Silverberg R F, Staquhn J G, Swain M R, Yorke H W, Zhang X L. Scientific motivation and technology requirements for the SPIRIT and SPECS far-infrared/submillimeter space interferometers. In: Proceedings of SPIE 4013, UV, Optical, and IR Space Telescopes and Instruments. International Society for Optics and Photonics, 2000, 36–47
5. Phillips T G, Keene J. Submillimeter astronomy (heterodyne spectroscopy). Proceedings of the IEEE, 1992, 80(11): 1662–1678
6. Majumdar A K. Advanced Free Space Optics (FSO): A Systems Approach. New York: Springer, 2014
7. Liu H B, Chen Y, Bastiaans G J, Zhang X C. Detection and identification of explosive RDX by THz diffuse reflection spectroscopy. Optics Express, 2006, 14(1): 415–423
8. Leahy-Hoppa M R, Fitch M J, Zheng X, Hayden L M, Osiander R. Wideband terahertz spectroscopy of explosives. Chemical Physics Letters, 2007, 434(4–6): 227–230
9. Davies A G, Burnett A D, Fan W, Linfield E H, Cunningham J E. Terahertz spectroscopy of explosives and drugs. Materials Today, 2008, 11(3): 18–26
10. Federici J F, Schulkin B, Huang F, Gary D, Barat R, Oliveira F, Zimdars D. Thz imaging and sensing for security applications—explosives, weapons and drugs. Semiconductor Science and Technology, 2005, 20(7): S266–S280
11. Tonouchi M. Cutting-edge terahertz technology. Nature Photonics, 2007, 1(2): 97–105
12. Roobottom C A, Mitchell G, Morgan-Hughes G. Radiation-reduction strategies in cardiac computed tomographic angiography. Clinical Radiology, 2010, 65(11): 859–867
13. Alexandrov B S, Gelev V, Bishop A R, Usheva A, Rasmussen K O. DNA breathing dynamics in the presence of a terahertz field. Physics Letters A, 2010, 374(10): 1214–1217
14. Siegel P H, Pikov V. Impact of low intensity millimetre waves on cell functions. Electronics Letters, 2010, 46(26): 70–72
15. Chen J, Chen Y, Zhao H, Bastiaans G J, Zhang X C. Absorption coefficients of selected explosives and related compounds in the range of 0.1-2.8 THz. Optics Express, 2007, 15(19): 12060–12067
16. Zhang X C, Shkurinov A, Zhang Y. Extreme terahertz science. Nature Photonics, 2017, 11(1): 16–18
17. Lee Y S. Principles of Terahertz Science and Technology. New York: Springer, 2009
18. Auston D H. Picosecond optoelectronic switching and gating in silicon. Applied Physics Letters, 1975, 26(3): 101–103
19. Tani M, Matsuura S, Sakai K, Nakashima S. Emission characteristics of photoconductive antennas based on low-temperature-grown GaAs and semi-insulating GaAs. Applied Optics, 1997, 36 (30): 7853–7859
20. Auston D H, Cheung K P, Smith P R. Picosecond photoconducting hertzian dipoles. Applied Physics Letters, 1984, 45(3): 284–286
21. Ropagnol X, Khorasaninejad M, Raeiszadeh M, Safavi-Naeini S, Bouvier M, Côté C Y, Laramée A, Reid M, Gauthier M A, Ozaki T. Intense THz Pulses with large ponderomotive potential generated from large aperture photoconductive antennas. Optics Express, 2016, 24(11): 11299–11311
22. Hafez H A, Chai X, Ibrahim A, Mondal S, Férachou D, Ropagnol X, Ozaki T. Intense terahertz radiation and their applications. Journal of Optics, 2016, 18(9): 093004
23. Boyd R W. Nonlinear Optics. Oxford: Elsevier, 2008
24. Kitaeva G Kh. Terahertz generation by means of optical lasers. Laser Physics Letters, 2008, 5(8): 559–576
25. Reimann K. Table-top sources of ultrashort Thz pulses. Reports on Progress in Physics, 2007, 70(10): 1597–1632
26. Rice A, Jin Y, Ma X F, Zhang X C, Bliss D, Larkin J, Alexander M. Terahertz optical rectification from $< 110 >$ zinc-blende crystals. Applied Physics Letters, 1994, 64(11): 1324–1326
27. Yang K H, Richards P L, Shen Y R. Generation of far-infrared radiation by picosecond light pulses in $LiNbO_3$. Applied Physics Letters, 1971, 19(9): 320–323
28. Hebling J, Almasi G, Kozma I, Kuhl J. Velocity matching by pulse front tilting for large area THz-pulse generation. Optics Express, 2002, 10(21): 1161–1166
29. Hebling J, Yeh K L, Hoffmann M C, Bartal B, Nelson K A. Generation of high-power terahertz pulses by tilted pulse-front excitation and their application possibilities. Journal of the Optical Society of America B, Optical Physics, 2008, 25(7): B6–B19
30. Fülöp J A, Pálfalvi L, Klingebiel S, Almási G, Krausz F, Karsch S, Hebling J. Generation of sub-mJ terahertz pulses by optical rectification. Optics Letters, 2012, 37(4): 557–559
31. Hirori H, Doi A, Blanchard F, Tanaka K. Single-cycle terahertz pulses with amplitudes exceeding 1 mV/cm generated by optical rectification in $LiNbO_3$. Applied Physics Letters, 2011, 98(9): 091106
32. Zhang X C, Ma X F, Jin Y, Lu T M, Boden E P, Phelps P D, Stewart K R, Yakymyshyn C P. Terahertz optical rectification from a nonlinear organic crystal. Applied Physics Letters, 1992, 61(26): 3080–3082
33. Hauri C P, Ruchert C, Vicario C, Ardana F. Strong-field single-cycle THz pulses generated in an organic crystal. Applied Physics

Letters, 2011, 99(16): 161116
34. Shalaby M, Hauri C P. Demonstration of a low-frequency three-dimensional terahertz bullet with extreme brightness. Nature Communications, 2015, 6(1): 5976
35. Hamster H, Sullivan A, Gordon S, White W, Falcone R W. Subpicosecond, electromagnetic pulses from intense laser-plasma interaction. Physical Review Letters, 1993, 71(17): 2725–2728
36. Cook D J, Hochstrasser R M. Intense terahertz pulses by four-wave rectification in air. Optics Letters, 2000, 25(16): 1210–1212
37. Dai J, Clough B, Ho I C, Lu X, Liu J, Zhang X C. Recent progresses in terahertz wave air photonics. IEEE Transactions on Terahertz Science and Technology, 2011, 1(1): 274–281
38. Kim K Y, Taylor A J, Glownia J H, Rodriguez G. Coherent control of terahertz supercontinuum generation in ultrafast laser–gas interactions. Nature Photonics, 2008, 2(10): 605–609
39. Wu Q, Zhang X C. Free-space electro-optic sampling of terahertz beams. Applied Physics Letters, 1995, 67(24): 3523–3525
40. Nuss M C, Auston D H, Capasso F. Direct subpicosecond measurement of carrier mobility of photoexcited electrons in gallium arsenide. Physical Review Letters, 1987, 58(22): 2355–2358
41. van Exter M, Fattinger C, Grischkowsky D. Terahertz time-domain spectroscopy of water vapor. Optics Letters, 1989, 14(20): 1128–1130
42. Morales G J, Lee Y C. Ponderomotive-force effects in a nonuniform plasma. Physical Review Letters, 1974, 33(17): 1016–1019
43. Liu K, Buccheri F, Zhang X C. Thz science and technology of micro-plasma. Physics (Chinese Wuli), 2015, 44: 497–502
44. Hamster H, Sullivan A, Gordon S, Falcone R W. Short-pulse terahertz radiation from high-intensity-laser-produced plasmas. Physical Review E: Statistical Physics, Plasmas, Fluids, and Related Interdisciplinary Topics, 1994, 49(1): 671–677
45. Löffler T, Jacob F, Roskos H G. Generation of terahertz pulses by photoionization of electrically biased air. Applied Physics Letters, 2000, 77(3): 453–455
46. D'Amico C, Houard A, Franco M, Prade B, Mysyrowicz A, Couairon A, Tikhonchuk V T. Conical forward THz emission from femtosecond-laser-beam filamentation in air. Physical Review Letters, 2007, 98(23): 235002
47. Amico C D, Houard A, Akturk S, Liu Y, Le Bloas J, Franco M, Prade B, Couairon A, Tikhonchuk V T, Mysyrowicz A. Forward THz radiation emission by femtosecond filamentation in gases: theory and experiment. New Journal of Physics, 2008, 10(1): 013015
48. Buccheri F, Zhang X C. Terahertz emission from laser induced microplasma in ambient air. Optica, 2015, 2(4): 366–369
49. Xie X, Dai J, Zhang X C. Coherent control of THz wave generation in ambient air. Physical Review Letters, 2006, 96(7): 075005
50. Kress M, Löffler T, Eden S, Thomson M, Roskos H G. Terahertz-pulse generation by photoionization of air with laser pulses composed of both fundamental and second-harmonic waves. Optics Letters, 2004, 29(10): 1120–1122
51. Clough B, Dai J M, Zhang X C. Laser air photonics: covering the "terahertz gap" and beyond. Zhongguo Wuli Xuekan, 2014, 52(1): 416–430
52. Chen Y, Yamaguchi M, Wang M, Zhang X C. Terahertz pulse generation from noble gases. Applied Physics Letters, 2007, 91 (25): 251116
53. Dai J, Liu J, Zhang X C. Terahertz wave air photonics: terahertz wave generation and detection with laser-induced gas plasma. IEEE Journal of Selected Topics in Quantum Electronics, 2011, 17 (1): 183–190
54. Dai J, Karpowicz N, Zhang X C. Coherent polarization control of terahertz waves generated from two-color laser-induced gas plasma. Physical Review Letters, 2009, 103(2): 023001
55. Kim K Y, Glownia J H, Taylor A J, Rodriguez G. Terahertz emission from ultrafast ionizing air in symmetry-broken laser fields. Optics Express, 2007, 15(8): 4577–4584
56. Karpowicz N, Zhang X C. Coherent terahertz echo of tunnel ionization in gases. Physical Review Letters, 2009, 102(9): 093001
57. You Y S, Oh T I, Kim K Y. Off-axis phase-matched terahertz emission from two-color laser-induced plasma filaments. Physical Review Letters, 2012, 109(18): 183902
58. Blank V, Thomson M D, Roskos H G. Spatio-spectral characteristics of ultra-broadband THz emission from two-colour photo excited gas plasmas and their impact for nonlinear spectroscopy. New Journal of Physics, 2013, 15(7): 075023
59. Manceau J M, Massaouti M, Tzortzakis S. Strong terahertz emission enhancement via femtosecond laser filament concatenation in air. Optics Letters, 2010, 35(14): 2424–2426
60. Liu J, Zhang X C. Terahertz-radiation-enhanced emission of fluorescence from gas plasma. Physical Review Letters, 2009, 103 (23): 235002
61. Liu J, Dai J, Chin S L, Zhang X C. Broadband terahertz wave remote sensing using coherent manipulation of fluorescence from asymmetrically ionized gases. Nature Photonics, 2010, 4(9): 627–631
62. Clough B, Liu J, Zhang X C. Laser-induced photoacoustics influenced by single-cycle terahertz radiation. Optics Letters, 2010, 35(21): 3544–3546
63. Cook D J, Chen J X, Morlino E A, Hochstrasser R M. Terahertz field-induced second-harmonic generation measurements of liquid dynamics. Chemical Physics Letters, 1999, 309(3–4): 221–228
64. Dai J, Xie X, Zhang X C. Detection of broadband terahertz waves with a laser-induced plasma in gases. Physical Review Letters, 2006, 97(10): 103903
65. Karpowicz N, Dai J, Lu X, Chen Y, Yamaguchi M, Zhao H, Zhang X C, Zhang L, Zhang C, Price-Gallagher M, Fletcher C, Mamer O, Lesimple A, Johnson K. Coherent heterodyne time-domain spectrometry covering the entire "terahertz gap". Applied Physics Letters, 2008, 92(1): 011131
66. Clough B, Dai J, Zhang X C. Laser air photonics: beyond the terahertz gap. Materials Today, 2012, 15(1–2): 50–58
67. Lu X, Karpowicz N, Chen Y, Zhang X C. Systematic study of broadband terahertz gas sensor. Applied Physics Letters, 2008, 93 (26): 261106
68. Zalkovskij M, Zoffmann Bisgaard C, Novitsky A, Malureanu R, Savastru D, Popescu A, Uhd Jepsen P, Lavrinenko A V. Ultrabroadband terahertz spectroscopy of chalcogenide glasses. Applied Physics Letters, 2012, 100(3): 031901
69. D'Angelo F, Mics Z, Bonn M, Turchinovich D. Ultra-broadband

THz time-domain spectroscopy of common polymers using THz air photonics. Optics Express, 2014, 22(10): 12475–12485
70. Yang Y, Mandehgar M, Grischkowsky D R. Broadband THz pulse transmission through the atmosphere. IEEE Transactions on Terahertz Science and Technology, 2011, 1(1): 264–273
71. Sun X, Buccheri F, Dai J, Zhang X C. Review of THz wave air photonics. In: Proceedings of SPIE 8562, Infrared, Millimeter-Wave, and Terahertz Technologies II. SPIE, 2012, 856202
72. Clough B, Liu J, Zhang X C. "All air-plasma" terahertz spectroscopy. Optics Letters, 2011, 36(13): 2399–2401
73. Berry M V, Balazs N L. Nonspreading wave packets. American Journal of Physics, 1979, 47(3): 264–267
74. Unnikrishnan K, Rau A R P. Uniqueness of the Airy packet in quantum mechanics. American Journal of Physics, 1996, 64(8): 1034–1035
75. Schiff L I. Quantum Mechanics. Oxford: McGraw-Hill Education (India) Pvt Limited, 1968
76. Durnin J. Exact solutions for nondiffracting beams. I. The scalar theory. Journal of the Optical Society of America A, Optics and Image Science, 1987, 4(4): 651–654
77. Durnin J, Miceli J Jr, Eberly J H. Diffraction-free beams. Physical Review Letters, 1987, 58(15): 1499–1501
78. McGloin D, Dholakia K. Bessel beams: diffraction in a new light. Contemporary Physics, 2005, 46(1): 15–28
79. Gutiérrez-Vega J C, Iturbe-Castillo M D, Chávez-Cerda S. Alternative formulation for invariant optical fields: Mathieu beams. Optics Letters, 2000, 25(20): 1493–1495
80. Bandres M A, Gutiérrez-Vega J C. Ince-Gaussian beams. Optics Letters, 2004, 29(2): 144–146
81. Siviloglou G A, Christodoulides D N. Accelerating finite energy Airy beams. Optics Letters, 2007, 32(8): 979–981
82. Siviloglou G A, Broky J, Dogariu A, Christodoulides D N. Observation of accelerating Airy beams. Physical Review Letters, 2007, 99(21): 213901
83. Abdollahpour D, Suntsov S, Papazoglou D G, Tzortzakis S. Spatiotemporal Airy light bullets in the linear and nonlinear regimes. Physical Review Letters, 2010, 105(25): 253901
84. Chong A, Renninger W H, Christodoulides D N, Wise F W. Airy–Bessel wave packets as versatile linear light bullets. Nature Photonics, 2010, 4(2): 103–106
85. Papazoglou D G, Efremidis N K, Christodoulides D N, Tzortzakis S. Observation of abruptly auto focusing waves. Optics Letters, 2011, 6(10): 1842–1844
86. Efremidis N K, Christodoulides D N. Abruptly autofocusing waves. Optics Letters, 2010, 35(23): 4045–4047
87. Papazoglou D G. Personal communication, 2015
88. Chremmos I, Efremidis N K, Christodoulides D N. Pre-engineered abruptly autofocusing beams. Optics Letters, 2011, 36(10): 1890–1892
89. Liu K, Koulouklidis A D, Papazoglou D G, Tzortzakis S, Zhang X C. Enhanced terahertz wave emission from air-plasma tailored by abruptly autofocusing laser beams. Optica, 2016, 3(6): 605–608
90. Koulouklidis A D, Papazoglou D G, Fedorov V Y, Tzortzakis S. Phase memory preserving harmonics from abruptly autofocusing beams. Physical Review Letters, 2017, 119(22): 223901
91. Papazoglou D G, Fedorov V Y, Tzortzakis S. Janus waves. Optics Letters, 2016, 41(20): 4656–4659
92. Panagiotopoulos P, Papazoglou D G, Couairon A, Tzortzakis S. Sharply autofocused ring-Airy beams transforming into non-linear intense light bullets. Nature Communications, 2013, 4(1): 2622
93. Polynkin P, Kolesik M, Roberts A, Faccio D, Di Trapani P, Moloney J. Generation of extended plasma channels in air using femtosecond Bessel beams. Optics Express, 2008, 16(20): 15733–15740
94. Polynkin P, Kolesik M, Moloney J V, Siviloglou G A, Christodoulides D N. Curved plasma channel generation using ultraintense Airy beams. Science, 2009, 324(5924): 229–232
95. Scheller M, Mills M S, Miri M A, Cheng W, Moloney J V, Kolesik M, Polynkin P, Christodoulides D N. Externally refuelled optical filaments. Nature Photonics, 2014, 8(4): 297–301
96. Matsubara E, Nagai M, Ashida M. Ultrabroadband coherent electric field from far infrared to 200 THz using air plasma induced by 10 fs pulses. Applied Physics Letters, 2012, 101(1): 011105
97. Manceau J M, Averchi A, Bonaretti F, Faccio D, Di Trapani P, Couairon A, Tzortzakis S. Terahertz pulse emission optimization from tailored femtosecond laser pulse filamentation in air. Optics Letters, 2009, 34(14): 2165–2167
98. Zhao J, Guo L, Chu W, Zeng B, Gao H, Cheng Y, Liu W. Simple method to enhance terahertz radiation from femtosecond laser filament array with a step phase plate. Optics Letters, 2015, 40(16): 3838–3841
99. Chu X. Evolution of an Airy beam in turbulence. Optics Letters, 2011, 36(14): 2701–2703
100. Dolev I, Kaminer I, Shapira A, Segev M, Arie A. Experimental observation of self-accelerating beams in quadratic nonlinear media. Physical Review Letters, 2012, 108(11): 113903
101. Dai J, Zhang X C. Terahertz wave generation from thin metal films excited by asymmetrical optical fields. Optics Letters, 2014, 39(4): 777–780
102. Roskos H G, Thomson M D, Kreß M, Löffler T. Broadband THz emission from gas plasmas induced by femtosecond optical pulses: From fundamentals to applications. Laser & Photonics Reviews, 2007, 1(4): 349–368
103. Oh T I, You Y S, Jhajj N, Rosenthal E W, Milchberg H M, Kim K Y. Scaling and saturation of high-power terahertz radiation generation in two-color laser filamentation. Applied Physics Letters, 2013, 102(20): 201113
104. Gorodetsky A, Koulouklidis A D, Massaouti M, Tzortzakis S. Physics of the conical broadband terahertz emission from two-color laser-induced plasma filaments. Physical Review A., 2014, 89(3): 033838
105. Talebpour A, Petit S, Chin S L. Re-focusing during the propagation of a focused femtosecond Ti:sapphire laser pulse in air. Optics Communications, 1999, 171(4–6): 285–290
106. Clough B, Karpowicz N, Zhang X C. Modulation of electron trajectories inside a filament for single-scan coherent terahertz wave detection. Applied Physics Letters, 2012, 100(12): 121105
107. Buccheri F, Liu K, Zhang X C. Terahertz radiation enhanced emission of fluorescence from elongated plasmas and microplasmas in the counter-propagating geometry. Applied Physics Letters, 2017, 111(9): 091103
108. Martin F, Mawassi R, Vidal F, Gallimberti I, Comtois D, Pepin H,

Kieffer J C, Mercure H P. Spectroscopic study of ultrashort pulse laser breakdown plasmas in air. Applied Spectroscopy, 2002, 56 (11): 1444–1452

109. Liu J, Zhang X C. Enhancement of laser-induced fluorescence by intense terahertz pulses in gases. IEEE Journal of Selected Topics in Quantum Electronics, 2011, 17(1): 229–236
110. Liu J, Dai J, Zhang X C. Ultrafast broadband terahertz waveform measurement utilizing ultraviolet plasma photoemission. Journal of the Optical Society of America B, Optical Physics, 2011, 28(4): 796–804

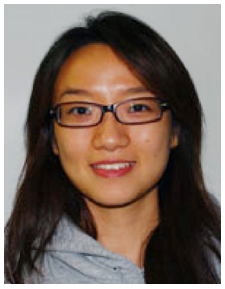

Kang Liu attended Fudan University, Shanghai, China and graduated with a Bachelor of Science degree in Physics in 2009. In 2011, she acquired a Diplôme d'Ingénieur (Engineering Diploma) from Institut d'Optique Graduate School, Palaiseau, France.

She began her doctoral studies in Optics at the University of Rochester in 2011 under the direction of Prof. Xi-Cheng Zhang with research topic on THz wave generation and detection. In 2015, she was granted a Worldwide Universities Network Researcher Mobility Travel Grant in support of her collaboration work with Prof. Stelios Tzortzakis. In the same year she received 1st place out of 148 applicants for the International IRMMW conference Best Student Presentation Award. In 2017, she was awarded the Rochester Precision Optics Graduate Project Award for her work in THz wave generation by ring-Airy beam induced plasma.

Email: kangliu.813@gmail.com

Pingjie Huang is an associate professor in the State Key Laboratory of Industrial Control Technology, College of Control Science and Engineering, Zhejiang University. He received his Ph.D. degree in mechanical engineering, with specialty in information sensing and instrumentation from Zhejiang University in 2004 and obtained his B.Sc. and M.Sc. degrees from Huazhong Agricultural University in 1996 and Xi'an University of Technology in 1999, respectively. His research interests mainly focus on advanced transducer and measurement, process and environmental information processing and event detection, and computer control system design and development, etc. He is a key member of the research group in Zhejiang University for early warning techniques and systems for urban water quality assurance, NDT&E of conductive structures, food products, water samples, and tissue etc. base on THz-TDS, UV-Vis, and ECT methods. In these five years, he has authored/co-authored more than 40 peer-reviewed papers and conference papers.

Supported by the CSC and starting from September 2017 for a period of one year, Pingjie Huang is a visiting scholar in Prof. Xi-Cheng Zhang's research group in The Institute of Optics, University of Rochester working on terahertz science and technology.

Email: huangpingjie@zju.edu.cn

Xi-Cheng Zhang, Parker Givens Chair of Optics, was Director of The Institute of Optics, University of Rochester (UR), NY, a foremost institution in optics and optical physics research and education (Jan. 2012–Jun. 2017). Prior to joining UR, he pioneered world-leading research in the field of ultrafast laser-based terahertz technology and optical physics at Rensselaer Polytechnic Institute, Troy NY ('92–'12). At RPI, he was the Eric Jonsson Professor of Science; Acting Head at the Department of Physics, Applied Physics & Astronomy; Professor of Electrical, Computer & System; and Founding Director of the Center for THz Research. He is co-founder of Zomega Terahertz Corp. With a B.S. degree ('82) from Peking University, he earned the M.S. ('83) and Ph.D. degrees ('86) in Physics from Brown University, RI.

Dr. Zhang served as Editor-in-Chief of *Optics Letters*, OSA ('14–'19). He is a Fellow of AAAS, APS, IEEE, OSA, and SPIE. Previous positions included visiting scientist at MIT ('85), Physical Tech. Division of Amoco Research Center ('87), EE Dept. at Columbia University ('87–'91); Distinguished Visiting Scientist at Jet Propulsion Laboratory, Caltech (2006). He holds 29 US patents, and is a prolific author and speaker.

His honors and awards include: Humboldt Prize ('18); Australian Academy of Science Selby Fellow ('17); IRMMW-THz Kenneth Button Prize ('14); OSA William F. Meggers Award ('12); IEEE Photonics Society William Streifer Scientific Achievement Award ('11); Rensselaer William H. Wiley 1866 Award ('09); Japan Society for the Promotion of Science Fellowship & NRC-CIAR Distinguished Visiting Scientist, Canada ('04); First Heinrich Rudolf Hertz Lecturer, RWTH, Aachen, Germany ('03). He also served two years as a Distinguished Lecturer of IEEE/LEOS. He received Rensselaer Early Career Award ('96), Research Corporation Cottrell Scholar Award ('95), NSF Early Career Award ('95), K.C. Wong Prize, K.C. Wong Foundation, Hong Kong ('95), NSF Research Initiation Award ('92). In '93–'94, he was an AFOSR-SRPF Fellow at Hanscom Air Force Base.

Email: xi-cheng.zhang@rochester.edu